Clustering of Low-Redshift ($z \leq 2.2$) Quasars from the Sloan Digital Sky Survey

Nicholas P. Ross,[1][*] Yue Shen,[2] Daniel E. Vanden Berk,[1] Andrew J. Connolly,[3]
Gordon T. Richards,[4] Donald P. Schneider,[1] Michael A. Strauss,[2]
Patrick B. Hall,[5] Neta A. Bahcall[2] et al.[6]

[1] *Department of Astronomy and Astrophysics, The Pennsylvania State University, 525 Davey Laboratory, University Park, PA 16802, U.S.A.*
[2] *Princeton University Observatory, Princeton, NJ 08544, U.S.A.*
[3] *Department of Astronomy, University of Washington, Box 351580, Seattle, WA 98195, U.S.A.*
[4] *Department of Physics, Drexel University, 3141 Chestnut Street, Philadelphia, PA 19104, U.S.A.*
[5] *Department of Physics and Astronomy, York University, Toronto, ON M3J 1P3, Canada*

7 August 2008

ABSTRACT

We present results for the Quasar 2-Point Correlation Function, ξ_Q, over the redshift range $0.3 \leq z \leq 2.2$, using data from the Sloan Digital Sky Survey (SDSS). Using nearly 50,000 quasars with spectroscopic redshifts from the Data Release 5 Quasar Catalogue, our study represents the largest sample used for this type of investigation to date. With our redshift range and the areal coverage of $\approx$5,700 deg^2, we sample nearly 40 h^{-3} Gpc^3 (comoving) of the Universe in volume, assuming the current ΛCDM cosmology.

Over our redshift range, we find that the redshift-space correlation function, $\xi(s)$, can still be described well by a traditional single power-law and find $s_0 = 5.95 \pm 0.45$ h^{-1} Mpc and $\gamma = 1.16^{+0.11}_{-0.16}$ over $1.0 \leq s \leq 25.0$ h^{-1} Mpc scales. Using the redshift-space distortions information present in the 2-D $\xi(\sigma, \pi)$ measurement, which is presented for the SDSS quasars for the first time, we calculate a value of $\beta(z = 1.27) = 0.43 \pm 0.01$ for the dynamical infall parameter. Using the projected correlation function, $w_p(\sigma)$, we calculate the real-space correlation length, $r_0 = 5.45^{+0.35}_{-0.45}$ and $\gamma = 1.90^{0.04+}_{-0.03}$, over $1.0 \leq \sigma \leq 130.0$ h^{-1} Mpc scales.

Splitting out sample up into redshift slices, we find evidence for very weak evolution of quasar clustering with the correlation length staying roughly constant at $s_0 \sim 6-7$ h^{-1} Mpc at $z < 2$, and only really increasing at redshifts greater than this. Comparing our results to recent deep X-ray surveys, we see a slight trend for X-ray selected AGN to be more clustered at $z \sim 1$ than our optically selected quasasr. However, using SDSS-RASS matched catalogues, we find no strong evidence for clustering strength on X-ray luminosity.

We compare our data to analytical models and find that quasars inhabit dark matter haloes of mass $M_{\rm halo} = 5 \times 10^{12} - 1 \times 10^{13} h^{-1} M_\odot$ from redshifts $z \sim 2.5$ (the peak of quasar activity) to $z \sim 0$ and thus, the typical halo mass for a quasar becomes relatively less massive, as you approach the current epoch. This result could be considered part of the larger picture of cosmic AGN "downsizing". We also find that a model of "uniform growth", where quasasr grow hierarchically from high-z until $z \sim 2$, with multiple epochs of activity at high redshifts, fits the current observational data well, out to $z = 6$. Finally, by comparing to recent high-z clustering measurements, of Lyman Break Galaxies, we suggest that these may be the progenitors of low, $z < 2$ redshift quasars and AGN.

Key words: clustering – quasars: general – cosmology: observations – large-scale structure of Universe. observations – Sky Surveys

[*] Email: npr@astro.psu.edu

1 INTRODUCTION

Understanding how and when the structures we see in the local Universe formed from the initial conditions present in the early Universe is one of the fundamental goals of modern observational cosmology. By tracing the evolution of clustering with cosmic epoch, we have the potential to understand the growth of structure and its relation to the energy and matter content of the Universe, including the relationship between the dark matter and the luminous galaxies and quasars that we observe.

As such, one of the primary science goals of the Sloan Digital Sky Survey (SDSS; York et al. 2000) was to measure the large-scale distribution of galaxies and quasars, and in particular, to determine the spatial clustering of quasars as a function of redshift. Shen et al. (2007) report on the clustering of high, $z \geq 2.9$ quasars from the SDSS; in this paper, we investigate the spatial clustering from redshift $z = 2.2$ to the present day, i.e. the evolution of quasar clustering over nearly 80% of the age of the Universe (the gap in redshift being a consequence of the optical selection techniques used in the SDSS).

Due to their high intrinsic luminosity, quasars are seen to large cosmological distances, and are thus good probes to investigate large-scale structure (LSS) and its evolution. However, until recently, quasar studies were plagued by low-number statistics, leading to shot noise, and investigations over small areas of sky that could be subject to sample variance. With the advent of large-area ($\gtrsim 1000 \deg^2$) surveys, with efficient selection techniques, these limitations have been overcome and the number of known quasars has increased by more than an order magnitude in the last decade, thanks mainly to the 2dF QSO Redshift Survey (2QZ; Boyle et al. 2000; Croom et al. 2004) and the SDSS. At present, there are over 100 000 objects spectroscopically classified as quasars in the SDSS. The latest quasar catalogue (Schneider et al. 2007) contains nearly 80 000 objects. Using the data from these large surveys, we are now in a position to make high-precision measurements of quasar clustering properties.

The two-Point Correlation Function, ξ, is a simple but powerful statistic commonly employed to describe LSS and is used to quantify the clustering properties of a given object (Peebles 1980). The observed value of ξ for quasars can be related to the underlying (dark) matter density distribution via

$$\xi(r)_{\mathrm{quasar}} = b_Q^2 \; \xi(r)_{\mathrm{matter}} \qquad (1)$$

where $\xi(r)_{\mathrm{matter}}$ is the mass correlation function and b_Q is the linear bias parameter for quasars, which links the visible quasars to the underlying matter density fluctuations. Although equation 1 defines b_Q, and there is evidence to believe b_Q is scale-independent (e.g. Scherrer & Weinberg 1998), we do not know *a priori* if this is the case.

With certain assumptions, the measurement and interpretation of the bias can lead to determination of the dark matter halo properties of quasars and potentially quasar lifetimes (t_q, Martini & Weinberg 2001; Haiman & Hui 2001). In the standard scenario, quasar activity is triggered by accretion onto a central, supermassive black hole (SMBH, e.g. Salpeter 1964; Lynden-Bell 1969; Rees 1984). Given that the growth of the SMBH is theoretically related to that of the underlying dark matter halo (Baes et al. 2003; Wyithe &

Loeb 2005; Wyithe & Padmanabhan 2006) and the halo properties are correlated with the local density contrast, clustering measurements provide an insight into quasar and black hole physics (da Ângela et al. 2008). This information includes constraining η, the fraction of the Eddington Luminosity at which quasars shine (Wyithe & Loeb 2005).

Early measurements of the quasar 2PCF, (e.g. Arp 1970; Hawkins & Reddish 1975; Osmer 1981; Shanks et al. 1983, 1987) measured statistically significant clustering on scales of $\sim$ a few h^{-1} Mpc, for both the quasar auto-correlation function and cross-correlation with galaxies. This result has been confirmed with data from the recent surveys, (e.g. Croom et al. 2005; Porciani et al. 2004). The Quasar 2PCF is typically fit to a single power-law of the form,

$$\xi(r) = (r/r_0)^{-\gamma} \qquad (2)$$

over the range $1 \; h^{-1}$ Mpc $\leq r \leq 100 \; h^{-1}$ Mpc, where r_0 is the correlation length quoted in comoving coordinates and γ the power-law slope. Typical correlation lengths and slopes for quasars at redshift $z \sim 1.5$ are $r_0 = 5 - 6 \; h^{-1}$ Mpc and $\gamma \sim 1.5$, respectively.

The evolution of the quasar correlation function was for a long time more disputed, with some authors claiming that quasar clustering, i.e. r_0, either decreased or only weakly evolved with redshift (e.g. Iovino & Shaver 1988; Croom & Shanks 1996), while others report an increase with redshift (e.g. Kundic 1997; La Franca et al. 1998). However, with the advent of the 2QZ Survey, the evolution of r_0 has been shown to evole with high significance, and that quasar clustering increases with redshift (Croom et al. 2001; Porciani et al. 2004; Croom et al. 2005). In particular, Croom et al. (2005) use 20 000 objects from the final 2QZ dataset to measure the redshift-space two-point correlation function, $\xi(s)$, over the redshift range, $0.3 < z < 2.2$. They find that the quasar clustering amplitude increases with redshift such that the integrated correlation function, $\bar{\xi}$, within 20 h^{-1} Mpc, is $\bar{\xi} = 0.26 \pm 0.08$ at $z = 0.53$, rising to $\bar{\xi} = 0.70 \pm 0.17$ at $z = 2.48$. The quasar bias is also derived, and is found to be a strong function of redshift, with an empirical dependence of

$$b_Q(z) = (0.53 \pm 0.19) + (0.289 \pm 0.035)(1 + z)^2. \qquad (3)$$

These values are used to derive the mean dark matter halo (DMH) mass occupied by quasars, which is found to be redshift-independent with $M_{DMH} = (3.0 \pm 1.6) \times 10^{12} h^{-1} M_\odot$. Independent analysis of the 2QZ data by Porciani et al. (2004) confirmed these findings.

Using the SDSS, Shen et al. (2007) found that redshift $2.9 \leq z \leq 5.4$ quasars are significantly more clustered than their $z \sim 1.5$ counterparts, having a real-space correlation length and power-law slope of $r_0 = 15.2 \pm 2.7 \; h^{-1}$ Mpc and $\gamma = 2.0 \pm 0.3$, respectively, over the scales $4 \; h^{-1}$ Mpc $\leq \sigma \leq 150 \; h^{-1}$ Mpc (where σ is the separation from the projected correlation function, $w_p(\sigma)$). Shen et al. (2007) also find that bias increases with redshift, with, $b_Q \sim 8$ at $z = 3.0$ and $b_Q \sim 16$ at $z = 4.5$.

Myers et al. (2006, 2007), also using the SDSS, examined the clustering of quasar candidates over $\sim 50 \; h^{-1}$kpc to $\sim 20 \; h^{-1}$ Mpc scales using photometrically identified catalogues (i.e. data where quasar redshifts have been assigned from photometric rather than spectral information, see e.g. Richards et al. 2001). They found that the linear

bias, b_Q increases with redshift, from $b_Q = 1.93$ at redshifts $0.4 \leq z < 1.0$ to $b_Q = 2.84$ at $2.1 \leq z < 2.8$.

Padmanabhan et al. (2008) measured the clustering of photometrically selected luminous red galaxies (LRGs) around a low, $0.2 < z < 0.6$, redshift sample of quasars, with both LRG and quasar samples coming from the SDSS. They determined a large-scale quasar bias $b_Q = 1.09 \pm 0.15$ at a median redshift of $z = 0.43$. This bias value corresponds to a mean halo mass of $M_{\mathrm{halo}} \sim 10^{12} h^{-1} M_\odot$, Eddington ratios of $0.01 < \eta < 1$ and quasar lifetimes of $< 10^7$ yrs. After taking into account measurement and interpretation subtleties, the results from Padmanabhan et al. (2008), are in qualitative agreement with those from Serber et al. (2006), who find that $M_i \leq -22$, $z \leq 0.4$ quasars are located in higher local overdensities than typical L^* galaxies. Serber et al. (2006) explain this by suggesting a picture in which quasars typically reside in L^* galaxies, but have a local excess of neighbors within $\sim 0.15 - 0.7 \ \ h^{-1}$ Mpc. This local density excess is likely to contribute to the triggering of quasar activity through mergers and other interactions. Hennawi et al. (2006), Myers et al. (2007) and Myers et al. (2008) reach similar conclusions by looking at the excess of pairs of quasars on $< 1 \ \ h^{-1}$ Mpc scales using binary quasars, with Hennawi et al. (2006) suggesting that the small-scale excess can likely be attributed to dissipative interaction events that trigger quasar activity in rich environments.

Recently, da Ângela et al. (2008) combined data from the 2QZ and the 2SLAQ Survey (2dF-SDSS LRG And QSO Survey; Croom et al. 2008), to investigate quasar clustering and break the "$L - z$ degeneracy". Due to the evolution of the quasar luminosity function, and the flux-limited nature of most quasar samples, there is a strong correlation between redshift and luminosity, i.e. a $L - z$ degeneracy. The extra dynamic range of the 2SLAQ QSO survey adds to the 2QZ by targetting fainter objectes over the same redshift range, da Ângela et al. (2008) estimate the mass of the dark matter haloes which quasars inhabit to be $\sim 3 \times 10^{12} h^{-1} M_\odot$ and that this halo mass does not evolve strongly with redshift nor depend on QSO luminosity. Their results also suggest that quasars of different luminosities may contain black holes of similar mass.

There has also been recent advances in theoretical predictions of the quasar correlation function and its evolution with redshift. Lidz et al. (2006) use numerical simulations of galaxy mergers to argue that although quasars at $z \sim 0$ and $z \sim 3$ reside in similar host halos, their clustering properties differ significantly. Specifically, quasars at $z \sim 0$ should be close to unbiased ($b_Q \sim 1$), while quasars at $z \sim 3$ are highly biased, with $b \sim 5$. The reason for this is simply that halos of mass $7.5 \times 10^{12} - 1.5 \times 10^{13} M_\odot$ correspond to rare, high-σ peaks at $z \sim 3$, and are thus highly clustered. On the other hand, the variance of the density field smoothed on the same mass scale is close to the collapse threshold at $z \sim 0$, and hence these low-redshift haloes faithfully trace the matter distribution near $z \sim 0$. These models have been updated in Hopkins et al. (2007, 2008) and describe well (with some important caveats which we shall return to in Section 4) the aforementioned observational results.

In this paper, we shall measure the quasar 2PCF for redshifts $z \leq 2.2$, using the largest sample of spectroscopically identified quasars to date. We will investigate the dependence of quasar clustering strength with redshift, and test

current galaxy formation and evolution theoretical models, which make strong predictions for the evolution of the linear bias, with redshift.

This paper is organised as follows. In Section 2 we present our data sample, mentioning several effects that could cause potential systematic measurement issues. In Section 3 we briefly describe the techniques involved in measuring the two-point correlation function. and in Section 4 we present our results In Section 5 we compare and contrast our evolutionary results with recent observations of objects and theoretical models and we conclude in Section 6. Three detailed appendices contain supplementary material, with Appendix A giving technical details for the SDSS, Appendix B describing our error analysis and Appendix C showing the results from the checks into systematics in the SDSS quasar 2PCF.

We assume the currently preferred flat, ΛCDM cosmology where $\Omega_{\mathrm{b}} = 0.042$, $\Omega_{\mathrm{m}} = 0.237$, $\Omega_\Lambda = 0.763$ (Sánchez et al. 2006; Spergel et al. 2007) and quote distances in h^{-1} Mpc to aid in ease of comparisons with previous results in the literature. Since we are measuring objects with redshifts resulting from the Hubble flow, all distances herein are given in comoving coordinates. Where a value of Hubble's Constant is assumed e.g. for Absolute Magnitudes, this will be quoted explicitly. Our magnitudes are based on the AB zero-point system (Oke & Gunn 1983).

2 DATA

Much care must be taken when constructing a dataset that is valid for a statistical analysis and we use this section, along with Appendix A to describe the various samples used to investigate potential systematic effects in our clustering measurements. In Appendix A we provide technical details for the SDSS, discussing the Catalogue Archive Server (CAS) and the SDSS Survey geometry.

2.1 The Sloan Digital Sky Survey

The SDSS uses a dedicated 2.5m wide-field telescope (Gunn et al. 2006) to collect light for 30 2k×2k CCDs (Gunn et al. 1998) over five broad bands - *ugriz* (Fukugita et al. 1996) - in order to image $\sim \pi$ steradians of the sky. The imaging data are taken on dark photometric nights of good seeing (Hogg et al. 2001) and are calibrated photometrically (Smith et al. 2002; Ivezić et al. 2004; Tucker et al. 2006), and astrometrically (Pier et al. 2003), and object parameters are measured (Lupton et al. 2001; Stoughton et al. 2002).

Using the imaging data, quasar target candidates are then selected for spectroscopic follow-up based on their colours, magnitudes and detection in the FIRST radio survey, with full details of the quasar selection given by Richards et al. (2002). Unless stated otherwise, all quoted SDSS photometry refers to Galactic extinction corrected data (corrections from the extinction models of Schlegel et al. 1998). Here we are concerned with only those quasars selected as primary targets, i.e. the main quasar selection, (Richards et al. 2002). Low-redshift, $z \lesssim 3$, quasar targets are selected based on their location in *ugri*-colour space and the high-redshift, $z \gtrsim 3$, objects in *griz*-colour space. The quasar candidate sample is flux-limited to $i = 19.1$ but since

high-redshift quasars are rare, objects lying in regions of colour-space corresponding to quasars at $z > 3$ are targetted to $i = 20.2$. Furthermore, if an unresolved, $i \leq 19.1$ SDSS object is matched to within 2" of a source in the FIRST catalogue, (Faint Images of the Radio Sky at Twenty centimetres; Becker et al. 1995), it is included in the quasar selection.

A tiling algorithm then assigns these candidates to specific spectroscopic plates, in order to maximise target completeness (Blanton et al. 2003). Each $3°$ spectroscopic plate holds 640 fibres and quasar candidates are allocated approximately 18 fibers deg^{-2}. Targetting priority is required since no two fibres can be placed closer than 55" (corresponding to ~ 0.7 h^{-1} Mpc at $\langle z \rangle = 1.27$, the mean redshift of our sample). The primary quasar candidates (where we define the primary sample below) were given targetting priority over the MAIN galaxy and LRG survey targets (Strauss et al. 2002; Eisenstein et al. 2001, respectively). However, excluding subtle effects due to gravitational lensing, (Scranton et al. 2005; Mountrichas & Shanks 2007), the LSS 'footprint' of these foreground galaxies should not affect our LSS quasar measurements. We also note that some targets e.g. brown dwarf and hot subdwarf standard star candidates, were given priority ahead of even the primary quasar candidates. However, since the surface density of these Galactic objects is very low ($\ll 1$ deg^{-2}), this decision should not have any significant impact on our results.

2.2   Quasar Samples

For our analysis, we use the Data Release Five (DR5; Adelman-McCarthy et al. 2007) and select quasars from the the latest version of the quasar catalogue (DR5Q; Schneider et al. 2007). This catalog consists of spectroscopically identified quasars that have luminosities larger than $M_i = -22.0$ (measured in the rest frame) and at least one emission line with FWHM larger than 1000 km s^{-1}. Every object in the DR5Q had its spectrum manually inspected and the catalogue has at most a small contamination of Type 2 QSOs, Seyferts or BL Lac objects. There are 77 429 confirmed quasars over the 5 740 deg^2 spectroscopic DR5 footprint, and the 65 660 DR5Q quasars with redshifts $z \leq 2.2$ will be the parent sample (defined below) we use in this investigation.

The $z \leq 2.2$ limit is set due to the fact that at this redshift, the "ultra-violet excess" (UVX) method of selecting quasars begins to fail due to the Lyα-forest suppressing flux as it moves through the SDSS u-band. Thus above this redshift and up to $z \approx 2.9$, the completeness of the survey is dramtically lowered as is discussed in depth by Richards et al. (2006). Therefore, althought we will present results in the redshift range $2.2 \leq z \leq 2.9$, we do so under caution, and will not include these measurements in any statistical analysis. The number of quasars used in this study represents a factor of > 2 increase in objects over the previous largest quasar survey, the 2QZ (Boyle et al. 2000; Croom et al. 2005). This increase in data allows us to improve constraints on theoretical models, as well as divide our sample while still retainting statistical power.

We construct two subsamples from DR5Q. The first is designated as the "PRIMARY" Sample, which will include those objects in the DR5Q which were targetted as
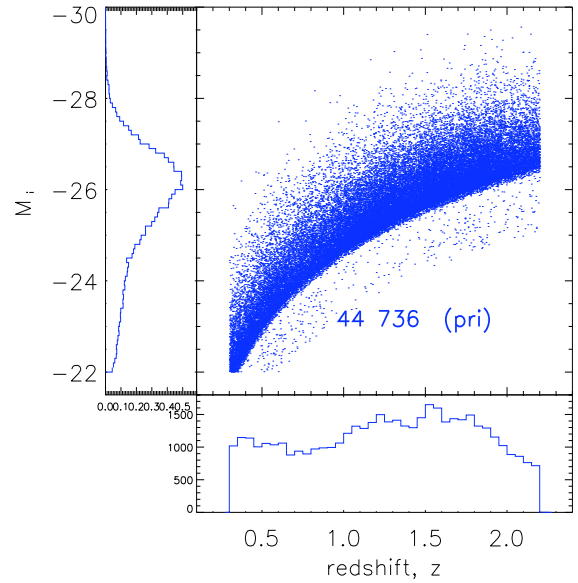

Figure 1. The SDSS DR5 Quasar $L - z$ plane for the PRIMARY sample. The affect of the apparent $i = 19.1$ magnitude limit can clearly be seen, and the objects that are fainter than this were those selected by the $z > 3$ algorithm. Please see http://www.astro.psu.edu/users/npr/DR5/ for further $L - z$ plots at full resolution.

primary quasar candidates, having satisfied one, or more, of the `TARGET_QSO`, `TARGET_HIZ` or `TARGET_FIRST` selections (see Stoughton et al. (2002), Section 4.8, for more details on these flags). The use of the primary sample is motivated by the fact that the SDSS quasar survey was designed to be complete in this selection, but no attempt was made at completeness for the other categories. In total there are 55 577 quasars in the DR5Q that had their target flags set to one (or more) of these primary flags, with 46 272 quasars satisfying our redshift cut-off (Table 1). We show the redshift-luminosity range for the PRIMARY sample in Figure 1.

Our second sample will be the "UNIFORM" sample, which is a subset of the PRIMARY sample. Full details of the selection for this sample are given in Richards et al. (2006) and Shen et al. (2007). In practice, this uniform sample selects quasars that were only targetted using the final quasar target selection algorithm, and as such, selects against data obtained from the earlier part of the SDSS, particularly in the EDR (Stoughton et al. 2002) and DR1 (Abazajian et al. 2003). There are 38 208 objects in total that are in this UNIFORM sub-sample, dropping to 31 290 when a redshift cut of $z \leq 2.2$ is applied.

We motivate the use of both the PRIMARY and UNIFORM sub-samples in our analysis as follows. We use the PRIMARY sample as we are keen to utilise as much of the data as possible, while keeping the completeness high. However, it is unclear what affect the change from the original target selection algorithm to the final target selection algorithm might have, with major effects expected only at $z > 3$. Thus, we use the UNIFORM sample to investigate this effect and find that these two samples give inconsistent results at large, > 60 h^{-1} Mpc. This is investigated further in Appendix C.

Sample Description		Area /deg^2	Number in sample	$z_{\min}$	$z_{\max}$	z_{med}
DR5Q		≈ 5740	77 429	0.078	5.414	1.538
"	$z \leq 2.9$		71 375	0.078	2.900	1.372
"	$0.3 \leq z \leq 2.9$		69 692	0.300	2.900	1.400
"	$z \leq 2.2$		65 660	0.078	2.200	1.278
"	$0.3 \leq z \leq 2.2$		63 977	0.300	2.200	1.306
PRIMARY		5713	55 577	0.080	5.414	1.543
"	$z \leq 2.9$		50 062	0.080	2.900	1.326
"	$0.3 \leq z \leq 2.9$		48 526	0.300	2.900	1.360
"	$z \leq 2.2$		46 272	0.080	2.200	1.234
"	**$0.3 \leq z \leq 2.2$**		**44 736**	**0.300**	**2.200**	**1.268**
UNIFORM		4013	38 208	0.084	5.338	1.575
"	$z \leq 2.9$		33 699	0.084	2.900	1.319
"	$0.3 \leq z \leq 2.9$		32 648	0.300	2.900	1.234
"	$z \leq 2.2$		31 290	0.084	2.200	1.354
"	**$0.3 \leq z \leq 2.2$**		**30 239**	**0.300**	**2.200**	**1.269**

Table 1. The SDSS Spectroscopic Quasar Samples used in our analysis, with minimum, maximum and median redshifts. The DR5Q is the catalogue presented in Schneider et al. (2007), while the PRIMARY and UNIFORM samples are described in Section 2. The results for the bold samples are given in Section 4.

Due to the evolution of the quasar luminosity function, and the flux-limited nature of the SDSS Quasar sample, there is a strong correlation between redshift and luminosity of our sample, often called the $L-z$ degeneracy. To separate the affects of any potential luminosity-dependent clustering and redshift-dependent clustering, one desires a large sample of objects, *at a fixed luminosity*, over the redshift-range of interest. Thus we aim to break the $L-z$ degeneracy, and plot our redshift-luminosity range for our PRIMARY sample in Figure 1.

2.3 Bad Fields and Reddening Systematics

The quasar correlation function is open to variation from a number of potential systematic effects. Two of these could be due to "bad fields" or dust reddening.

Since quasars are selected by their optical colors, we shall also perform checks on both our PRIMARY and UNIFORM samples to see what affect regions with poor photometry has on our clustering measurements. The definition of these "bad fields" is given by Richards et al. (2006) and Shen et al. (2007).

While all selection for the quasar sample is undertaken using dereddened colors (Richards et al 2001), if there remain systematic errors in the reddening model they can induce excess power into the clustering in a number of different ways. We present results in Appendix C to demonstrate how the effects described above do/do not seriously affect our $\xi(s)$ measurements and the interpretations based thereon.

3 TECHNIQUES

In this section we shall describe the techniques we shall use to calculate the Quasar $z \leq 2.2$ 2PCF. The 2PCF has been the subject of much scrutiny, e.g. Peebles (1980, 1993); Peacock (1999); Coles & Lucchin (2002); Martínez & Saar

(2002) and the interested reader is referred to those comprehensive texts for full details on the 2PCF.

3.1 Estimating the 2-Point Quasar Correlation Function

In practice, ξ is measured by comparing the actual quasar distribution to a catalogue of "random" quasars, which have the same selection function, angular mask and radial distribution as the data, but are spatially distributed in a "random" manner - i.e. have no LSS. The construction of this random sample shall be described in Section 3.3.

We use the estimator of Landy & Szalay (1993) to calculate ξ, as this has been found to be the most reliable estimator for 2PCF studies (Kerscher et al. 2000). We do, however, compare our results using the 'standard' estimator of Davis & Peebles (1983) and the estimator from Hamilton (1992). The three estimators are given by,

$$\xi_{LS}(s) = 1 + \left(\frac{N_{rd}}{N}\right)^2 \frac{DD(s)}{RR(s)} - 2\left(\frac{N_{rd}}{N}\right)\frac{DR(s)}{RR(s)} \quad (4)$$

$$\equiv \frac{\langle DD \rangle - \langle 2DR \rangle + \langle RR \rangle}{\langle RR \rangle} \quad (5)$$

$$\xi_{Std}(s) = \left(\frac{N_{rd}}{N}\frac{DD(s)}{DR(s)}\right) - 1, \quad (6)$$

and

$$\xi_{\mathrm{Ham}}(s) = \frac{DD(s) \cdot RR(s)}{DR(s)^2} - 1 \quad (7)$$

for the Landy-Szalay (LS), 'Standard' and Hamilton estimators respectively. Here N and N_{rd} are the number of data and random points in the sample, $DD(s)$ is the number of data-data pairs with separation between s and $s + ds$ in the given catalogue, $DR(s)$ is the number of data-random pairs and $RR(s)$ the number of random-random pairs. The angled brackets denote the suitably normalised pair counts,

since we employ at least twenty times more random points than data in order to reduce Poisson noise. We choose our bin widths to be $\Delta \log(s/\ h^{-1}\ \mathrm{Mpc}) = 0.1$ in size.

The measurement of a quasar redshift will not only have a (large) component due to the Hubble expansion, but also a component due to the intrinsic peculiar velocities associated with the individual quasar. The peculiar velocities can been seen in the redshift-space correlation function, both at small- and large-scales (see Section 4). The real-space correlation function is what would be measured in the absence of any redshift-space distortions. However, as noted in Shen et al. (2007, Appendix A), and Schneider et al. (2007), subtle effects creep into quasar redshift determination and redshift-errors of order $\Delta z = 0.001$ will potentially dominate our peculiar velocity signal.

3.2 The 2-D 2PCF, $\xi(\sigma, \pi)$, and the Projected Correlation Funcion, $w_p(\sigma)$

For ease of comparison against theoretical models (Section 5.2), we desire to know not only the redshift-space correlation function, but also the real-space correlation function (e.g. the real-space correlation function length, r_0 and slope, γ).

One can resolve the redshift-space separation, s, into two components, σ and π, where σ is the separation between two objects *perpendicular* to the line-of-sight and π is the separation *parallel* to the line-of-sight. Thus,

$$s^2 = \sigma^2 + \pi^2, \tag{8}$$

where $r_p \equiv \sigma$ is also found in the literature. The '2-D' redshift-space correlation function, $\xi(\sigma, \pi)$, can be calculated as before,

$$\xi_{\mathrm{LS}}(\sigma, \pi) = \frac{\langle DD(\sigma, \pi) \rangle - \langle 2DR(\sigma, \pi) \rangle + \langle RR(\sigma, \pi) \rangle}{\langle RR(\sigma, \pi) \rangle} \tag{9}$$

where the bin sizes are now chosen to be $\Delta \log(\sigma\ h^{-1}\ \mathrm{Mpc}) = \Delta \log(\pi\ h^{-1}\ \mathrm{Mpc}) = 0.2$.

Redshift-space distortions affect only the radial component of $\xi(\sigma, \pi)$; thus by integrating along the line-of-sight direction, π, we obtain the projected correlation function,

$$w_{\mathrm{p}}(\sigma) = 2 \int_0^\infty \xi(\sigma, \pi) \, d\pi. \tag{10}$$

In practice we set the upper limit on the integral to be $\pi_{\max} = 10^{1.8} = 63.1\ h^{-1}$ Mpc and show that although varying this limit does cause some difference to the deduced $w_{\mathrm{p}}(\sigma)$, it does not cause significant changes to the 2PCF over the scales of interest for our studies (Appendix B9).

The integral in equation 10 can be rewritten in terms of $\xi(r)$ (Davis & Peebles 1983),

$$w_{\mathrm{p}}(\sigma) = 2 \int_0^{\pi_{\max}} \frac{r\,\xi(r)}{\sqrt{(r^2 - \sigma^2)}} dr \tag{11}$$

If we assume that $\xi(r)$ is a power-law of the form, $\xi(r) = (r/r_0)^{-\gamma}$ (which, as we shall find later, is a fair assumption), then equation 11 can be integrated analytically, such that with $\pi_{\max} = \infty$,

$$w_p(\sigma) = r_0^\gamma \sigma^{1-\gamma} \left[\frac{\Gamma(\frac{1}{2})\,\Gamma(\frac{\gamma-1}{2})}{\Gamma(\frac{\gamma}{2})} \right] = r_0^\gamma \sigma^{1-\gamma} A(\gamma), \tag{12}$$
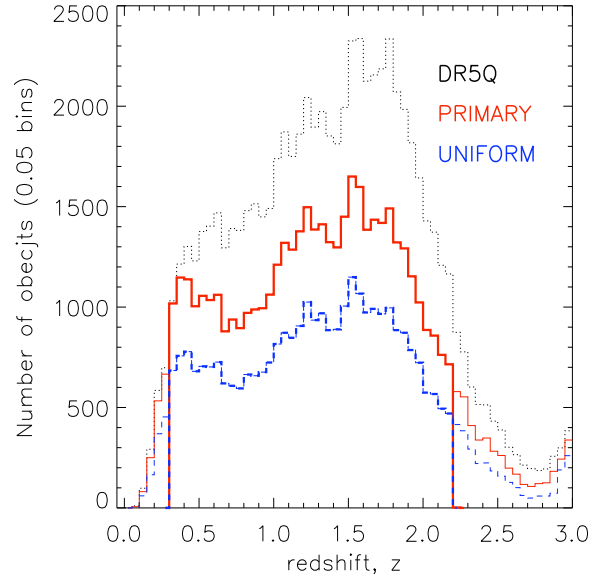
where $\Gamma(x)$ is the Gamma function.

Figure 2. The SDSS DR5 Quasar $N(z)$. The solid (red) histogram show the quasar redshift distribution for the PRIMARY sample, while the dashed (blue) histogram show the redshift distribution for the UNIFORM sample. The thin lines for both PRIMARY and UNIFORM, do not include the $0.3 \leq z \leq 2.2$ cuts. As a comparison, the full DR5Q is given by the dotted (black) histogram.

In linear theory and in the absence of small-scale velocites and redshift errors, the redshift-space and real-space correlation function can be related via

$$\xi(s) = \xi(r) \left(1 + \frac{2}{3}\beta + \frac{1}{5}\beta^2 \right), \tag{13}$$

where

$$\beta = \frac{\Omega_{\mathrm{m}}^{0.55}}{b} \tag{14}$$

parametrizes the 'flattening' at large-scales of the correlation function due to the infall of matter from underdense to overdense regions. We again note that equations 13 and 14 are only in the limit of linear peculiar velocities and the value of β has traditionally been measured via fits to observed data (e.g. Kaiser 1987; Peacock et al. 2001; Hawkins et al. 2003; Ross et al. 2007; Guzzo et al. 2008).

3.3 Construction of the Random Catalogue

As mentioned above, to calculate ξ in practice, one needs to construct a random catalogue of points that mimics the data in every way, bar its clustering signal. Here we describe the construction of such a "random" catalogoue for our samples.

3.3.1 Angular Mask

The angular mask of the SDSS has a describable, but non-trivial geometry. As such, one of the main challenges involved in producing a catalogue of "random" points, is to mimic the angular geometry completeness of the observational survey. Here again we use our two samples, PRIMARY

and UNIFORM, as our data, and thus aim to build to angular completeness masks for both. Full technical details of the construction of our angular mask are given in Appendix A.

3.3.2 Radial Distribution

Figure 2 shows the $N(z)$ distribution of the DR5Q Quasars from our samples. We fit a high-order polynomial to both the PRIMARY and UNIFORM samples which we use to generate the random sample redshift distribution. This method has proved reliable in previous quasar clustering studies (e.g. Croom et al. 2005; da Ângela et al. 2008).

3.3.3 Fibre Collisions and the Impact on Small-Scale Structure

Due to the design of the SDSS fibres and plates, no two spectroscopic fibres can be separated by less than 55". Thus, if two objects are closer than this separation, they will not be fibred in one plate observation. We use the PhotoObjAll catalogue (Appendix A) to investigate which potential quasars would not have been observed due to fibre collisions, and find that for DR5, *on average*, only ~ 1 object deg^{-2} is affected by this limitation. Thus, although we acknowledge that we are potentially missing quasar pairs (or indeed triplets, quads etc.) on small, ≤ 1 h^{-1} Mpc scales, we do not currently correct for this noting that Hennawi et al. (2006) and Myers et al. (2008) have dealt with quasar clustering on these scales in much greater detail.

3.4 Errors and Covariances

Recent correlation studies (e.g. Scranton et al. 2002; Zehavi et al. 2002; Myers et al. 2006; Ross et al. 2007) have employed three main methods, *Poisson, Field-to-Field* and *Jackknife* to estimate errors associated with correlation function measurements. The 'simplest' of these is the Poisson error described by Peebles (1973), and is the Poisson noise owing to the number of pairs in the sample,

$$\sigma_{\mathrm{Poi}} = \frac{1 + \xi(s)}{\sqrt{\mathrm{DD(s)}}}. \tag{15}$$

This should be valid at smaller scales where the number of pairs is small and most pairs are independent (Shanks & Boyle 1994; Croom & Shanks 1996). However, as reported in Myers et al. (e.g. 2005); Ross et al. (e.g. 2007), the Poisson error can under-estimate a measurements error when compared to e.g. the Field-to-Field or Jackknife errors at larger scales, where quasars pairs are not independent. For this work, we will not report any Field-to-field errors, but instead concentrate on a jackknife resampling procedure in order to calculate the full covariance matrix. Full details of the jackknife procedure, including the geometry of the subsamples used, is given in Appendix B.

4 RESULTS

4.1 SDSS Quasar Redshift-Space 2-Point Correlation Function, $\xi(s)$ ($0.30 \leq z \leq 2.2$)

The 2-Point redshift-space correlation function for the SDSS DR5Q UNIFORM sample over the redshift interval $0.3 <$
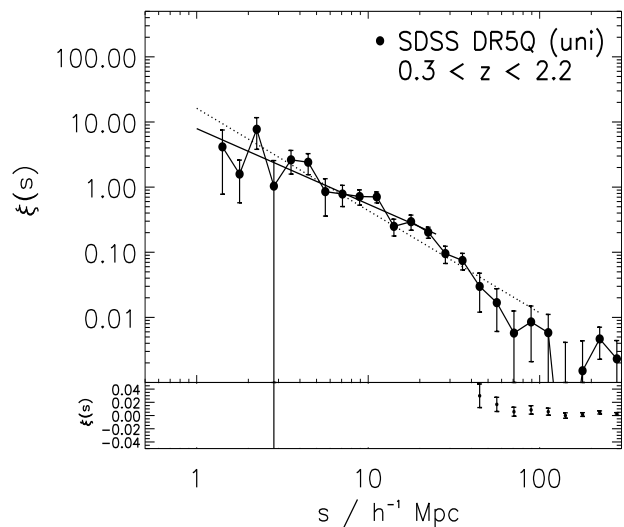

Figure 3. The SDSS Quasar redshift-space 2PCF, $\xi(s)$, from the UNIFORM sample filled (black) cirles. The solid line shows the best fit single power-law model over $1 \leq s \leq 25.0$ h^{-1} Mpc, while the dotted line shows the best fits single power-law model over $1 \leq s \leq 100.0$ h^{-1} Mpc. The lower panel shows the $\xi(s)$ behaviour near zero on a linear scale. The quoted errorbars are jackknife errors from the diagonalised Covariance matrix.
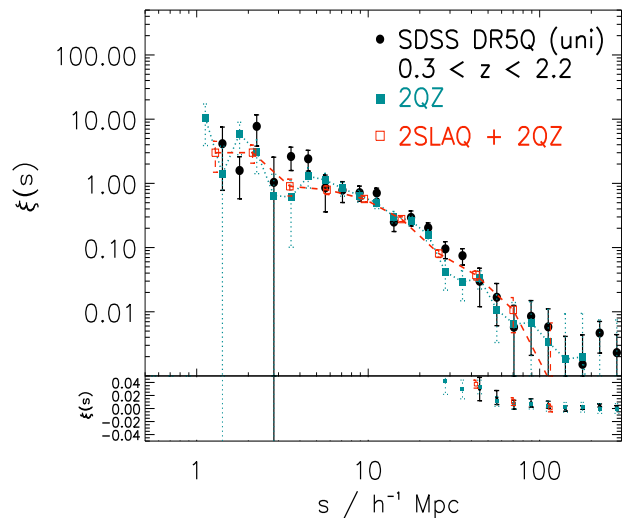

Figure 4. The Quasar redshift-space 2PCF, $\xi(s)$, from the UNIFORM sample as in Fig. 3. Also shown are the redshift-space correlation functions from the 2QZ (cerulean) filled squares, dotted line, (Croom et al. 2005) and the 2SLAQ QSO (red) open squares, dashed line (da Ângela et al. 2008) surveys.

$z < 2.2$ is given in Figure 3. The errorbars are jackknife errors from the diagonalised Covariance matrix, i.e. $\sigma_i = C_{ii}$.

We start by fitting a simple, single power-law model of the form from Equation 2. We find that a single-power law with a redshift-space correlation lenght of $s_0 = 5.95 \pm 0.45$ and power-law slope of $\gamma = 1.16^{+0.11}_{-0.08}$ provides a good description of the data over the scales $1.0 \leq s \leq 25.0$ h^{-1} Mpc (solid line, Fig. 3). Here a value of $\chi^2 = 11.5$ is obtained with 11 degrees of freedoms (dof). A less suitable fit is found at

larger scales. Over the range $1.0 \leq s \leq 100.0$ h^{-1} Mpc, the best fit model now has a similar correlation length, $s_0 = 5.90 \pm 0.30$ but a steeper power-law slope, $\gamma = 1.57^{+0.04}_{-0.05}$ (dotted line, Fig. 3). The χ^2 for this model is 32.8 with 15 dof. Note for the power-law model fit over $1.0 \leq s \leq 100.0$ h^{-1} Mpc, the data systematically deviate from the model, due to the effects of redshift-distortions, with a "flattening" of the data compared to the model at both small, $s \lesssim 5$ h^{-1} Mpc, and large, $s \gtrsim 40$ h^{-1} Mpc, scales.

In Figure 4, we show the redshift-space correlation function $\xi(s)$ from two other recent surveys, the 2QZ (Croom et al. 2005), filled (cerulean) squares and the 2SLAQ QSO (da Ângela et al. 2008) survey, open (red) squares. The analysis by da Ângela et al. (2008) actually uses data from both the 2QZ and 2SLAQ QSO surveys and as such, the filled and open squares will have data common to both.

Both the 2QZ and 2SLAQ QSO surveys cover very similar redshift ranges to our $z < 2.2$ SDSS DR5Q UNIFORM sample. The 2QZ covers a smaller, $\approx 750 \deg^2$, area than the SDSS but has a roughly similar number of quasars to our sample, since it reaches to a deeper limiting magnitude of $b_J = 20.85$ (or $g \approx 20.80$ and $i \sim 20.42$). The 2SLAQ QSO survey has a smaller area again, $\approx 180 \deg^2$ and goes a magnitude deeper than the 2QZ to $g = 21.85 (i \approx 21.45)$ resulting in 8 500 redshift $0.3 < z < 2.2$ quasars.

The agreement in the correlation function between surveys over 1 h^{-1} Mpc $\leq s \leq 100$ h^{-1} Mpc scales is impressive but not necessarily unexpected, since we are essentially sampling the same type of objects i.e. luminous AGN, powered by supermassive black holes accreting at or near their Eddington limits, quite possibly in similar mass environments (see Section 5). However, the fact the we measure similiar clustering lengths, and hence assuming these objects reside in dark matter haloes of similar mass, for surveys which have > 2 magnitudes difference in limiting depth, might be evidence to suggest that variation in quasar luminosity is due to a variation in SMBH fueling, rather than a variation in SMBH mass. We shall return to this subject in Section 5.

In Figure 5 we show the very large, $s \leq 3000$ h^{-1} Mpc, scale $\xi(s)$, with jackknife errors, using the LS estimator (we present $\xi(s)$ using the Standard and Hamilton estimators at these very large scales in Appendix C). We see that apart from one data point at $s \approx 400$ h^{-1} Mpc, the redshift-space correlation function is consistent with $\xi(s) = 0$ at scales greater than ~ 300 h^{-1} Mpc, to within one sigma. A χ^2 test comparing the data to $\xi(s) = 0$ over the range of $100 \leq s < 1000$ and $100 \leq s < 3000$ gives $\chi^2 = 8.2$ (18 dog) and $\chi^2 = 25.3$ (54 dog) respectively. Our rms scatter is ± 0.001, which compares well to the 2QZ value of ± 0.002, seeing as with $\sim 50\%$ more data, we have roughly double the pair counts at these very large scales. We do also observe that from ~ 500 h^{-1} Mpc to around 2000 h^{-1} Mpc, there is a strong trend for positive values of $\xi(s)$. However, we find no reason to draw any conclusions from this apparent feature. At scales great than ~ 3000 h^{-1} Mpc, we rapidly start losing Quasar-Quasar DD pairs and hence set this to be the maximum scale we can probe with our current survey data.
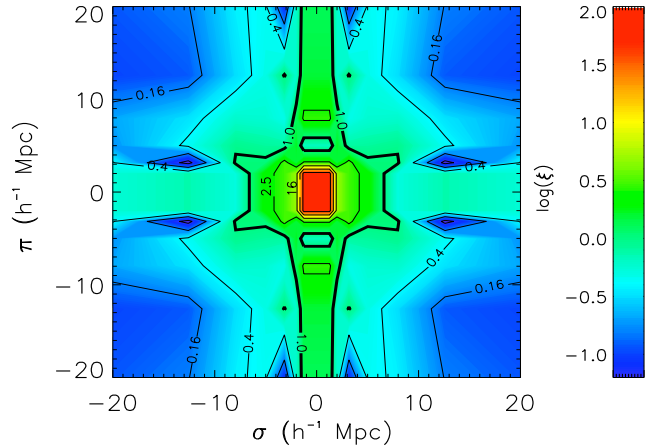

Figure 6. The SDSS DR5 Quasar $\xi(\sigma, \pi)$. The contours give lines of constant ξ, and $\delta \log \xi = 0.4$ between contours, with $\log \xi = 1.6$ the highest value at the centre of the plot. The thick contour is $\xi = 1.0$. This is the first time $\xi(\sigma, \pi)$ has been reported for the SDSS Quasar sample.

4.2   SDSS Quasar 2-D 2-Point Correlation Function, $\xi(\sigma, \pi)$ $(0.30 \leq z \leq 2.2)$

Figure 6 shows the SDSS DR5 Quasar 2-D redshift-space correlation function $\xi(\sigma, \pi)$ for the UNIFORM sample, over $0.3 \leq z \leq 2.2$. The redshifts-space distortions in the clustering signal - seen as deviations for a concentric circle representation - are immediately apparent. At small σ, the random peculiar motions of quasars cause an elongation of the clustering signal along the line-of-sight direction, π. This is the well-known and so called 'Fingers-of-God' effect. At large scales in σ, the predominanty effect is the coherent infall caused by bulk flows, which causes a 'squashing' of the $\xi(\sigma, \pi)$ contours along the parallel π direction. We note that although these effects have been seen in other quasar surveys, e.g. the 2QZ, this is the first time the 2-D clustering has been measured for the SDSS Quasar sample.

Extending equation 14, we can estimate the parameter βz, which takes into account the large-scale effects of the linear redshift-space distortions, from $\beta(z) = \Omega_{\mathrm{matter}}(z)^{0.55} b(z)$, where $\Omega_{\mathrm{matter}}(z)$ is the value of the matter density at redshift z and b is again the linear bias mentioned previously. As we shall find in Section 5.3, the linear bias for the DR5Q UNIFORM sample is $b(z = 1.27) = 2.06 \pm 0.03$ and thus $\beta(z = 1.27) = 0.43 \pm 0.01$. This compares well and is consistent with the value measure from the 2QZ survey, $\beta(z = 1.4) = 0.50^{+0.13}_{-0.15}$ (Outram et al. 2001; da Ângela et al. 2005). However, due to the much smaller space density of quasars compared to that of e.g. galaxies, the S/N of clustering measurement on small, i.e. the scales covered in Fig. 6, is much less. Thus we suggest that although this is the highest S/N quasar measurement of β to date, our formal errorbar might still be under-representative. Further cosmological information can be extracted from the Quasar 2D $\xi(\sigma, \pi)$ measurement (e.g. Hoyle et al. 2002; da Ângela et al. 2005, 2008), however, we leave these analyses to a future paper.
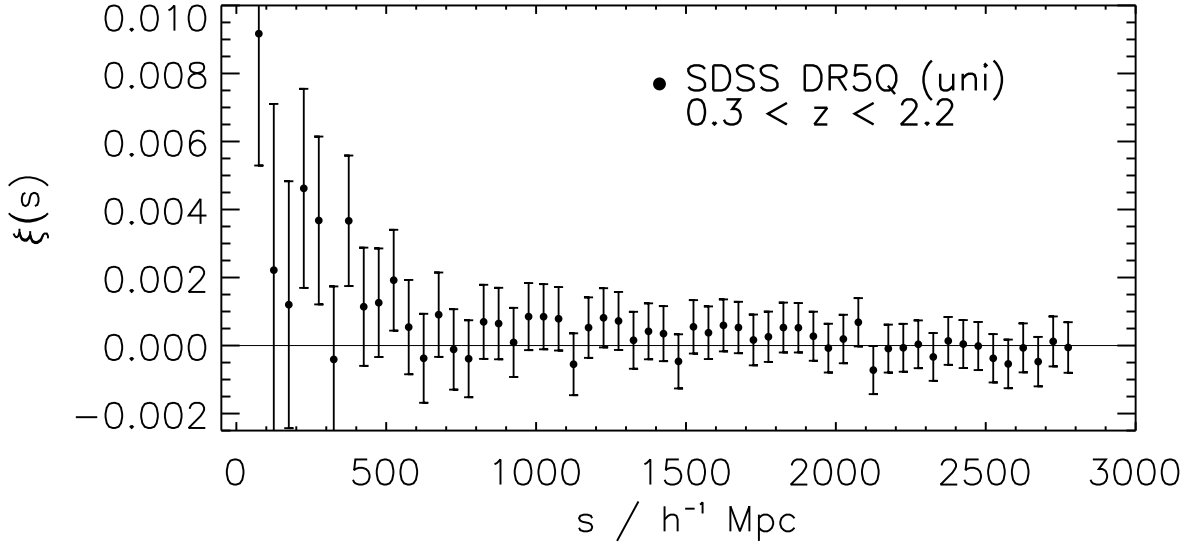
Figure 5. The SDSS Quasar redshift-space 2PCF, $\xi(s)$, for our UNIFORM sample over the redshift range $0.3 \leq z \leq 2.2$ at very large scales. Jackknife errors are plotted and the data are consistent with $\xi(s) = 0$ out to scales of $s \sim 3000$ h^{-1} Mpc. Above these scales, there is a rapid drop-off in Quasar-Quasar 'DD' pairs.
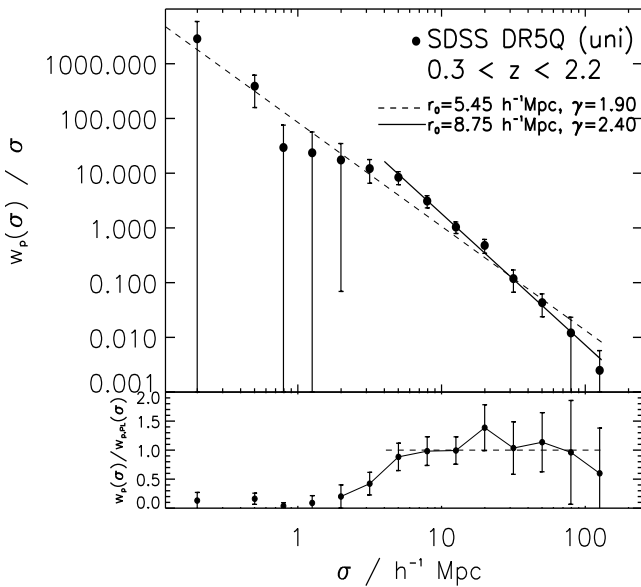

Figure 7. The SDSS Quasar redshift-space 2PCF, $w_p(\sigma)$. The broken line shows the best fit single power-law to the data over our full range of scales, $0.1 < \sigma < 130.0$ h^{-1} Mpc. Here, the real-space correlation length is $r_0 = 5.45^{+0.35}_{-0.45}$ with a slope, $\gamma = 1.90^{+0.04}_{-0.03}$. Restricting the range to $4.0 < \sigma < 130.0$ h^{-1} Mpc, the best-fit values now become $r_0 = 8.75^{+0.35}_{-0.50}$ and $\gamma = 2.40^{+0.07}_{-0.10}$. In the lower panel, we show the ratio of the data divided by our power-law model over $4.0 < \sigma < 130.0$ h^{-1} Mpc.

4.3 SDSS Quasar Projected 2-Point Correlation Function

In Figure 7, we show the projected 2-point correlation function, $w_p(\sigma)$, calculated using equation 11. The reported error bars are jackknife errors, using the same jackknife area subsamples as for the $\xi(s)$ calculation. Since we are now ende-
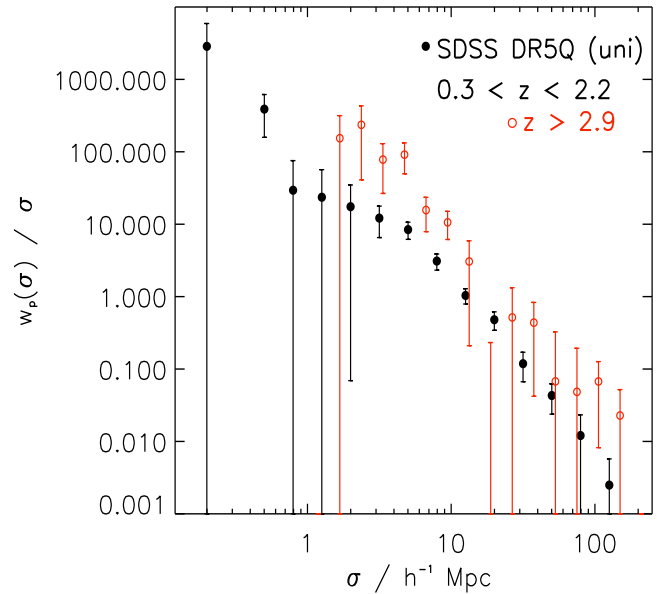
Figure 8. The SDSS Quasar redshift-space 2PCF, $w_p(\sigma)$. We see clearly that the higher redshift sample at redshifts $z > 2.9$ have a higher clustering amplitude than the data at lower, $z < 2.2$ redshifts. This is strong evidence that the high-z population are more biased tracers of the underlying matter distribution.

vouring to fit power-laws of the form, $\xi(r) = (r/r_0)^\gamma$ (equation 12), we plot $w_p(\sigma)/\sigma$ as the ordinate axis. We find the best fitting single power-law to the SDSS Quasar $w_p(\sigma)/\sigma$ data to be $r_0 = 5.45^{+0.35}_{-0.45}$ and $\gamma = 1.90^{+0.04}_{-0.03}$ over our full range of scales, $0.1 < \sigma < 130.0$ h^{-1} Mpc. This provides a somewhat adequate fit giving a value of $\chi^2 = 22.02$ with 12 degrees of freedom. We place a strong reminder that due to fibre collisions, measurements at scales of $\sigma \lesssim 1$ h^{-1} Mpc are to be treated with much caution. Restricting the range
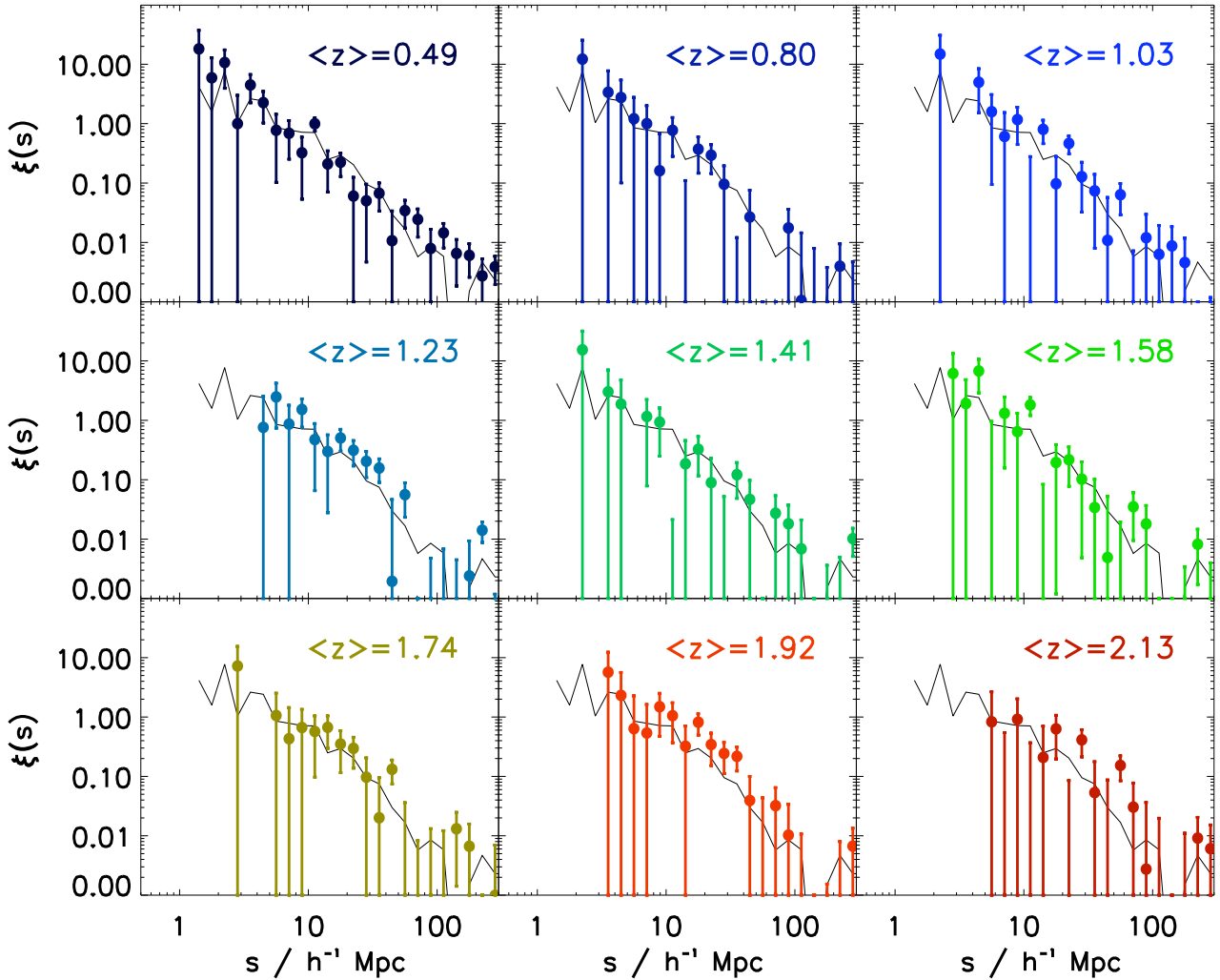
Figure 9. The SDSS DR5 Quasar redshift-space 2PCF, $\xi(s)$, and its evolution with redshift. The thin (black) line in each panel is $\xi(s)$ for the full DR5Q UNIFORM sample, over $0.30 < z < 2.20$. The quoted errorbars are Poisson (see text for justification).

to $4.0 < \sigma < 130.0$ h^{-1} Mpc, we find the best fit power-law values of has an increased real-space correlation length of $r_0 = 8.75^{+0.35}_{-0.50}$ and a steeper slope of $\gamma = 2.40^{+0.07}_{-0.10}$. As can be seen, this power-law is a more acceptable fit having $\chi^2 = 3.47$ with 6 dof. In the bottom panel we divide the data by this steeper, higher amplitude power-law and see negligable deviation over the scales we fit.

In Figure 8, we show the projected 2-point correlation function $w_p(\sigma)/\sigma$ for the SDSS Quasars at $0.3 \leq z \leq 2.2$ and the high, $z > 2.9$ redshift quasar measurements from Shen et al. (2007), given by open (red) circles. We see clearly the high redshift SDSS quasars having a much larger clustering amplitude than the lower redshift sample. The consequences of this are discussed in detail in Shen et al. (2007). This gives us strong evidence that high redshift quasars are a more biased population than their lower redshift counter-parts. As such, we shall continue our investigations into the evolution of clustering by now splitting our sample into different redshift bins.

4.4   Evolution of the SDSS Quasar Correlation Function

Figures 9, and 10 show the evolution of the redshift-space, $\xi(s)$, and the projected, $w_p(\sigma)$, 2PCF, using the SDSS DR5 UNIFORM Quasar sample.

We plot both $\xi(s)$ and $w_p(\sigma)$ for sub-samples of the UNIFORM data, with the relevent redshift limits given in Table 2. Here we choose the redshift slices so that we match those of the 2QZ Survey given by Croom et al. (2005). Our survey generally has 50% more data in each redshift bin. However, since the 2QZ selects QSO candidates on the basis of their stellar appearance on photographic plates, low-redshift quasars with detectable host galaxies on the plate could be preferentially deselected from the final 2QZ catalogue. Thus, this might explain why the SDSS Quasar UNIFORM sample has a larger proportion of low, $z \lesssim 0.5$, redshift quasars. This manifests itself in our $0.30 \leq z < 0.68$ redshift bin by having more objects than any other redshift slice or its 2QZ counterpart. We fit power-law models of the form given by equation 2, over the ranges $1.0 \leq s \leq$
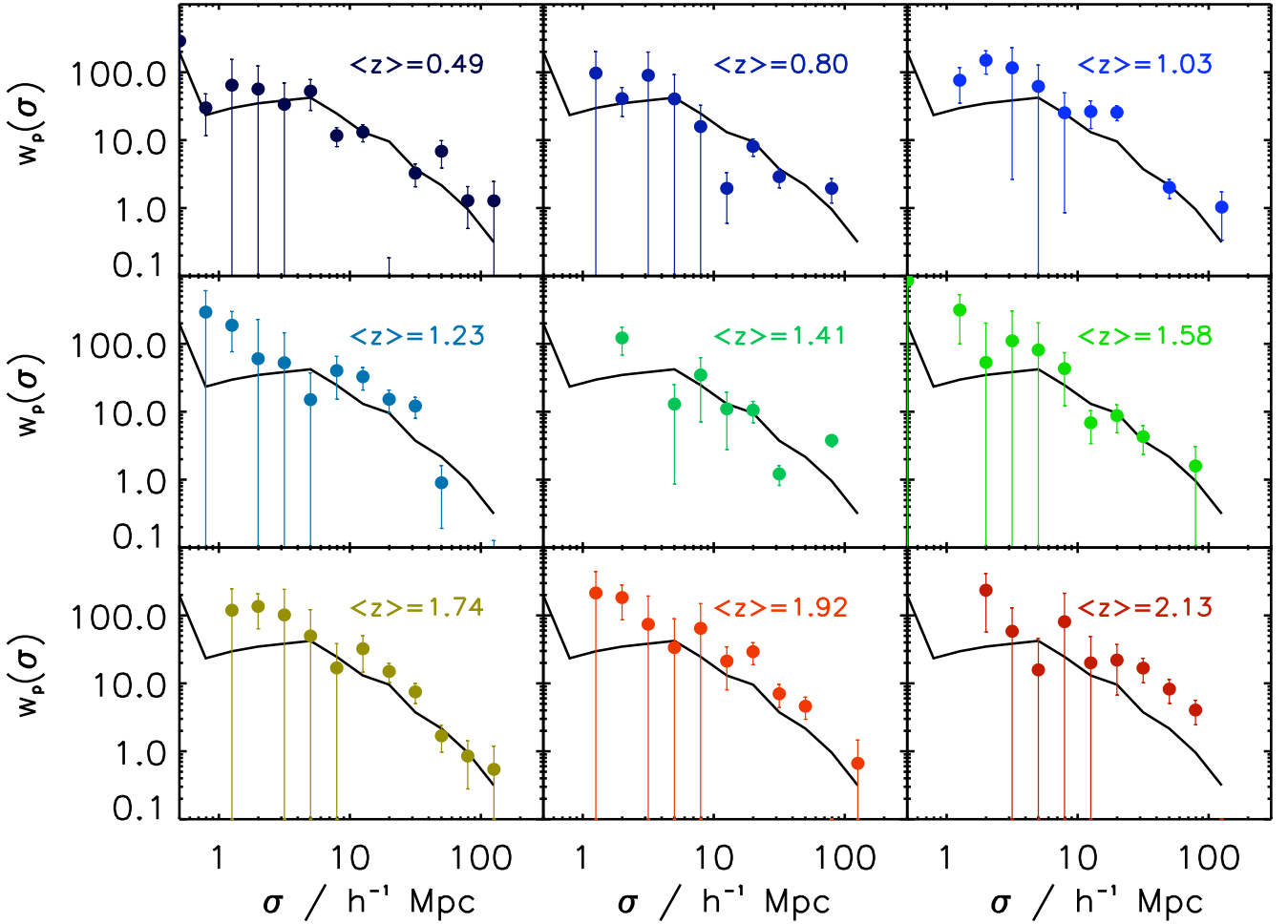
Figure 10. The SDSS DR5 Quasar projected 2PCF, $w_p(\sigma)$, and its evolution with redshift. The thin (black) line in each panel is $w_p(\sigma)$ for the full DR5Q UNIFORM sample, over $0.30 < z < 2.2$. The quoted errorbars are scaled jackknifes.

25.0 h^{-1} Mpc expect for our $2.02 \leq z < 2.20$ bin, where to get finite constraints, we fit to a $s_{\max} = 100$ h^{-1} Mpc. The best fit parameters and corresponding 1σ errors are given in Table 2. We shall plot the evolution of s_0 as a function of redshift in Figure 11 in Section 5.

In Fig. 9, we show measurements for $\xi(s)$ for 9 out of our 11 redshift slices. We exclude the lowest and highest redshift bins due to issues with low number statistics and completeness. The measurement of $\xi(s)$ for the full redshift range measurement is given by the thin (black) line in each panel. We quote Poisson errors as these are approximately equal to jackknife errors on scales where the number of DD pairs is less than the number of quasars in the (sub-)sample. This scale is $s \sim 50 - 100$ h^{-1} Mpc for the sub-samples given here. Fig. 10 has the same form as Fig. 9. However, here we quote jackknife errors (scaled using the $w_p(\sigma)/\sigma$ measurements above) as we find Poisson errors vastly underestimate the errorbars for projected correlation function measurements.

In both plots the trend is for the amplitude of the correlation function to increase with increasing redshift. However,

the evolution is not particularly strong for $z \lesssim 2$. The clearest evidence for the increase in clustering strength comes from the $\langle z \rangle = 1.92$ and $\langle z \rangle = 2.13$ redshift slices, in particular from the $w_p(\sigma)$ measurements. We see that the data from these points clearly have a higher clustering amplitude than the overall sample. We also note that the $\xi(s)$ data show a trend to 'lose' quasar-quasar DD pairs at the smallest separation, as the redshift increases. This is hardly surprising since the length-scale obscured due to the 55" fibre collisions will increase from $s \sim 0.2$ h^{-1} Mpc at $z = 0.5$ to $s \sim 1$ h^{-1} Mpc at $z = 2$.

5 EVOLUTION OF GALAXY, AGN AND QUASAR CLUSTERING

5.1 The Redshift-Space Evolution

The most comparable study of quasar clustering to our own is that presented by Croom et al. (2005) for the 2QZ survey. Thus, we start by comparing our results with theirs and Figure 11 shows the evolution of the redshift-space correlation

z-interval	$\bar{z}$	$N_{\rm gals}$	Bolo. Lum (10^{46} ergs^{-1})	s_0 (h^{-1} Mpc)	γ_s	χ^2	ν	r_0 (h^{-1} Mpc)
0.30,2.20	1.269	30 239	3.73	5.95 ± 0.45	$1.16^{+0.11}_{-0.16}$	11.5	11	$5.45^{+0.35}_{-0.45}, \gamma = 1.90^{+0.04}_{-0.03}$
				$^a5.90 \pm 0.30$	$1.57^{+0.04}_{-0.05}$	32.8	17	$8.75^{+0.35}_{-0.50}, \gamma = 2.40^{+0.07}_{-0.10}$
0.08,0.30	0.235	1 051	0.17	$6.90^{+1.35}_{-1.50}$	$1.37^{+0.41}_{-0.31}$	2.6	9	8.80 ± 0.85
0.30,0.68	0.488	5 404	0.49	$6.05^{+0.45}_{-0.65}$	$1.67^{+0.23}_{-0.24}$	12.2	11	6.44 ± 0.57
0.68,0.92	0.801	3 001	1.45	$7.05^{+1.15}_{-1.45}$	$1.90^{+0.60}_{-0.60}$	6.2	8	6.40 ± 0.64
0.92,1.13	1.029	3 365	2.18	$2.68^{+1.42}_{-1.28}$	$0.57^{+0.14}_{-0.15}$	9.4	7	8.20 ± 0.84
1.13,1.32	1.228	3 623	2.94	$7.10^{+1.45}_{-1.65}$	$1.00^{+0.30}_{-0.25}$	2.5	6	7.31 ± 0.82
1.32,1.50	1.412	3 332	3.81	$6.05^{+1.35}_{-1.85}$	$2.13^{+0.87}_{-0.78}$	6.1	7	6.78 ± 0.93
1.50,1.66	1.577	3 405	4.69	$6.10^{+1.40}_{-1.60}$	$1.67^{+0.81}_{-0.50}$	13.5	8	7.71 ± 0.82
1.66,1.83	1.744	3 240	5.81	$7.70^{+1.70}_{-1.90}$	$1.11^{+0.39}_{-0.31}$	1.0	6	7.34 ± 0.71
1.83,2.02	1.917	2 970	7.37	$7.43^{+2.37}_{-2.43}$	$0.84^{+0.41}_{-0.30}$	2.5	7	9.38 ± 0.79
2.02,2.20	2.104	1 899	9.67	$^a3.65^{+1.60}_{-1.85}$	$1.10^{+0.29}_{-0.15}$	8.7	10	10.51 ± 0.96
2.20,2.90	2.462	2 409	13.49	$10.75^{+2.15}_{-3.42}$	$2.60^{+0.6}_{-1.1}$	0.2	4	13.51 ± 1.80

Table 2. Evolution of the redshift-space, s_0 and real-space, r_0 correlation lengths. For s_0, both the correlation length and power-law slope were allowed to vary. All samples were fitted over the range $1.0 \leq s \leq 25.0$ h^{-1} Mpc, unless otherwise noted with ^{a}, where the range was $1.0 \leq s \leq 100.0$ h^{-1} Mpc. For the redshift slice subsamples, the calculation of r_0 was made by fitting a single power-law to $w_p(\sigma)$, over the scales $1.0 \leq \sigma \leq 130.0$ h^{-1} Mpc, while keeping the power-law index fixed at $\gamma = 2.0$.

length, s_0, with both redshift and the age of the Universe (adopting the cosmology given at the end of Section 1.) We immediately notice three main features.

First, the clustering strength as given by s_0 remains reasonably constant with redshift out to $z \sim 2$, which is equivalent to approximately 75% of the history of the Universe. This trend was also noted in Fig. 9. Second, the correlation length is measured to be $s = 6 - 7$ h^{-1} Mpc for bright, optically identified quasars in the SDSS, up to $z \sim 2$.

Third, the results from our study using the SDSS DR5Q UNIFORM quasar sample and the 2QZ are in good agreement over the full redshift range, with the evolution being very similarly described by both surveys. With the exception of the two points at $z = 0.49$ and $z = 2.13$, one might suggest that the SDSS points are systematically higher than the 2QZ data. For the lower redshift of the two points in question, we find that although the best-fit power-law value has $s_0 = 2.68^{+1.42}_{-1.28}$ and $\gamma = 0.57^{+0.14}_{-0.15}$, from studying the joint-error contours on both parameters, a value of $s_0 \approx 6$ h^{-1} Mpc and $\gamma \approx 1.3$ is also consistent with the data. For the higher redshift point, we find that sitting over the scales $1.0 \leq s \leq 25.0$ h^{-1} Mpc gives a best fitting value of $s_0 \sim 5$ h^{-1} Mpc, more in line with the general trend, but does not provide enough information to adequately constrain the power-law slope. We thus fit over $1.0 \leq s \leq 100.0$ h^{-1} Mpc for this redshift slice (Table 2). The trend for the SDSS points to be higher than the 2QZ maybe be explained by the main difference between the surveys, i.e. the limiting magnitude. However, this would potentially hint at a luminosity-dependence on clustering, evidence for which is weak (Croom et al. 2005; Porciani & Norberg 2006). We leave further discussion of this topic to our companion paper Shen et al. (2008, in prep.).

The filled (red) star in Fig. 11 is from the study by Wake et al. (2004) who use a sample of 13 605 narrow-line AGNs in the redshift range $0.055 < z < 0.2$ from the first Data Release of the SDSS. These authors find that, the AGN autocorrelation function is consistent with the observed galaxy autocorrelation function over 0.2 to greater than 100 h^{-1} Mpc scales. Furthmore, they show that the AGN 2PCF is dependent on the luminosity of the narrow [O III] emission line ($L_{\rm [OIII]}$), with low $L_{\rm [OIII]}$ AGNs having a higher clustering amplitude than high $L_{\rm [OIII]}$ AGNs. This measurement is consistent with lower activity AGNs residing in more massive galaxies than higher activity AGNs with $L_{\rm [OIII]}$ providing a good indicator of SMBH fueling rate. As such, it is very interesting to note that our lowest redshift quasar clustering data point is, within the uncertainties, consistent with the measurement from Wake et al. (2004). We use the term 'quasar' here loosely, as for this low redshift bin, the bolometric luminosity is 1.7×10^{45} ergs s^{-1}, a factor of 20 lower compared to our full sample (Table 2) and where the luminosity for a single line is $L_{\rm [OIII]} \sim 4 \times 10^{44}$ ergs s^{-1} in the AGN sample. This would then suggest, and be consistent with, an "AGN cosmic downsizing" scenario, which has become a popular explanation of observations in recent years (e.g. Steffen et al. 2003; Ueda et al. 2003; Heckman et al. 2004). We shall return to this in Section 5.4 below.

5.2 The Real-Space Evolution

In Figure 12, we compare our measurements of the real-space correlation length, r_0, to those recently published in the literature. We calculate our values for r_0 by fitting our $w_p(\sigma)$ measurements using equation 12. Motivated by the fits in Fig. 7, we hold the power-law index fixed at $\gamma = 2.0$.

Myers et al. (2006) were the first to make a measurement of the clustering of quasars using SDSS data, and also report on its evolution. These authors use $\sim 80\,000$ photometrically classified from the KDE (kernel density estimation) catalogue from Richards et al. (2004). As such, the r_0 measurements from Myers et al. (2006) are given by the open (red) squares in Fig. 12, are in very good agreement with our own data (we plot the data from their Table 1, from the 'De-projected r_0' section and the $0.75 \leq r < 89$ h^{-1} Mpc row). The lowest redshift Myers et al. (2006) point, may have a
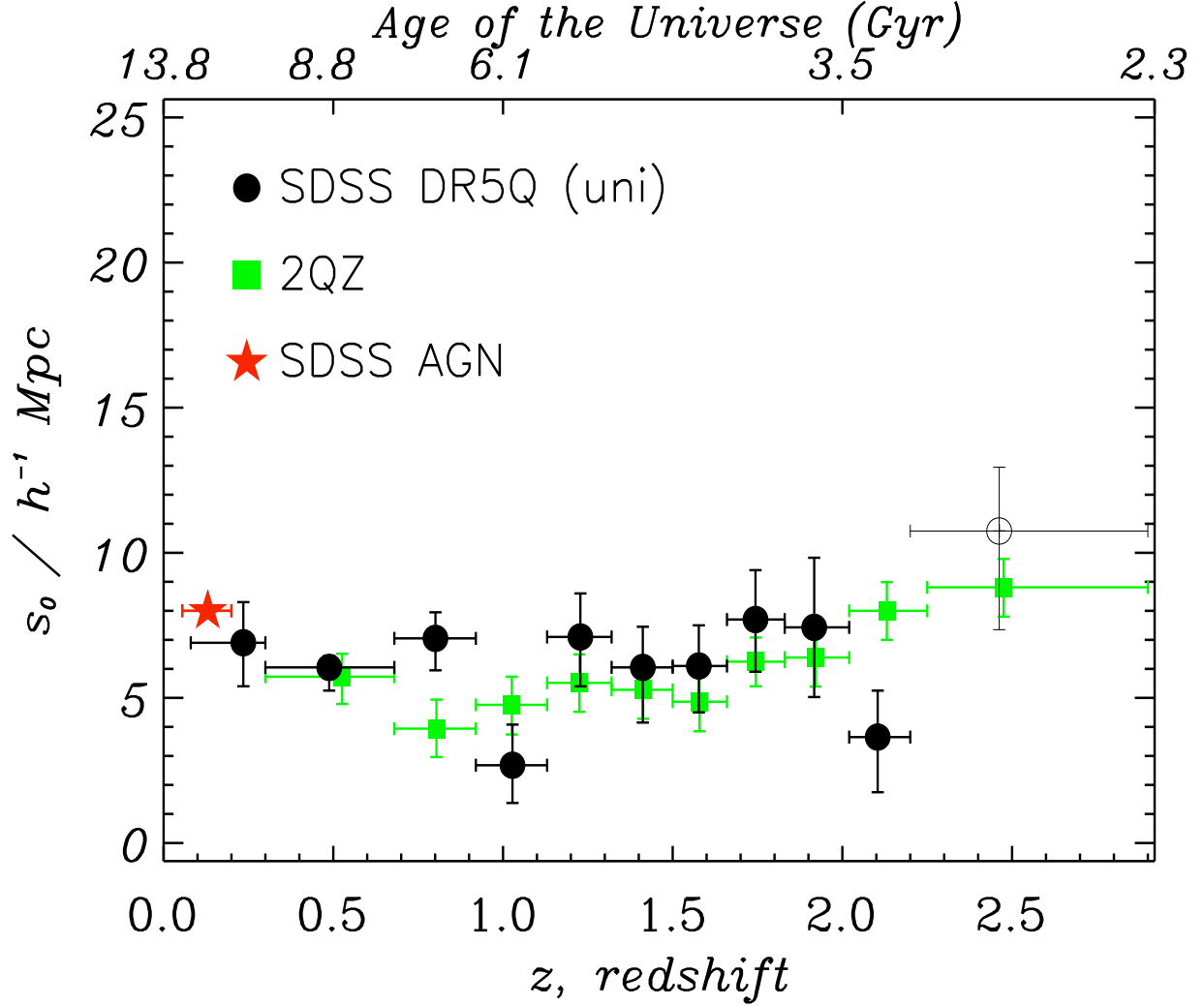
Figure 11. Evolution of the redshift-space correlation length, s_0, up to redshift $z = 2.9$. The (black) filled circles are from the DR5Q UNIFORM sample (this work); the (green) filled squares are from the 2QZ (Croom et al. 2005); the (red) filled star is from a measurement of AGN clustering at low, $z < 0.2$, redshift by Wake et al. (2004).

low clustering amplitude compared to our two low-z bins at $z = 0.49$ and $z = 0.80$, but this measurement is still consistent with our data given the 1σ uncertainties on both datasets.

Coil et al. (2007) calculate the cross-correlation between $\sim 30\,000$ redshift $0.7 < z < 1.4$ galaxies observed as part of the DEEP2 galaxy redshift survey (Davis et al. 2001, 2003), and quasars over the same redshift range. In total there are 36 SDSS quasars and 16 quasars identified from the DEEP2 survey itself over the 3 deg^2 covered by the DEEP2. Coil et al. (2007) find that $r_0 \sim 3.4 \pm 0.7$ h^{-1} Mpc for the quasar-galaxy cross-correlation (ξ_{QG}), and assuming $\xi_{QG} = \sqrt{(\xi_{QQ}.\xi_{GG})}$, $\xi_{GG} = 3.75$ h^{-1} Mpc and a linear bias (discussed below), gives a quasar clustering scale of $r_0 \sim 3.1 \pm 0.6$ h^{-1} Mpc. We show this as an open (purple) diamond in Fig. 12. Although still consistent with the low-redshift measurement of Myers et al. (2006), it is at odds with our measurements. One possible explanation is that only 12 out of 36 of the SDSS quasars selected meet the magnitude limit of $i = 19.1$ for the primary SDSS low-

redshift target selection algorithm Richards et al. (2002, as discussed in detail in Section 2) and used in our anaylsis. Although by measuring the galaxy-quasar cross-correlation, one does not need the quasar selection function information explicitly, the incompleteness of the SDSS at magnitudes fainter than $i = 19.1$ may still impact a correlation function measurement. Further investigations of this discrepancy and comparisons to other recent high, $z > 1$, galaxy survey clustering measurements are left to a future paper (Ross et al. 2008, in prep.).

A very interesting comparison can also be made using our optical, wide survey, quasar measurements to that of recent deep X-ray surveys, the latter of which are particularly well suited to finding intrinsically less luminous, potentially obscured objects at high-redshift (Brandt & Hasinger 2005). An immediate caveat we place in the following comparison is that the SDSS DR5Q surveys over ~ 4000 deg^2, while the largest solid angle of the current deep X-ray surveys is of order $\lesssim 1$ deg^2.

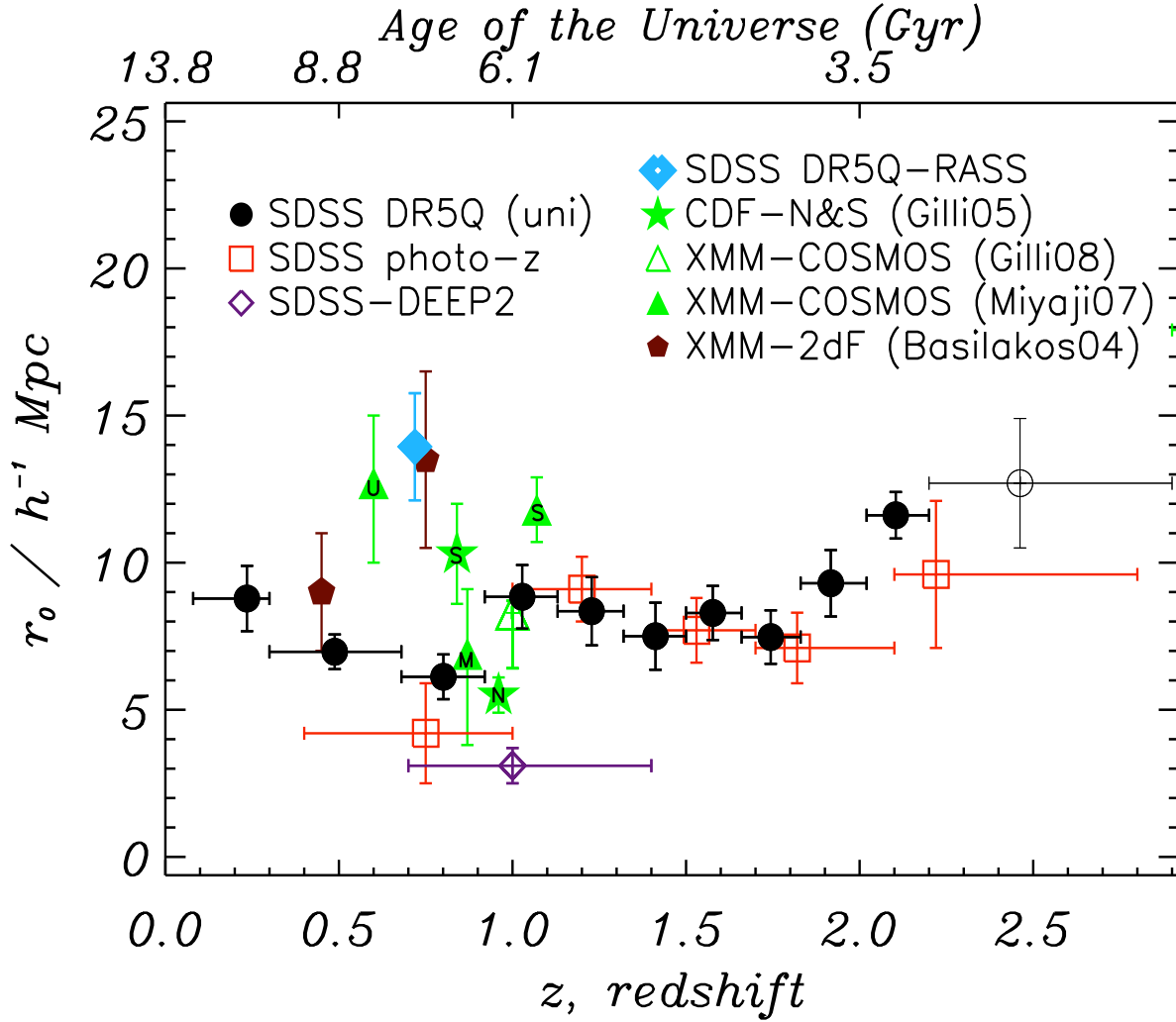Basilakos et al. (2004) estimate the r_0 using the an-

Figure 12. Evolution of the real-space correlation length, r_0, up to redshift $z = 2.9$. The filled (black) circles are from the DR5Q UNIFORM sample (this work); the open (red) squares are from the photometric sample of SDSS quasars from Myers et al. (2006); data from the *Chandra* Deep Fields (Gilli et al. 2005) are shown by filled (green) 5-pointed stars with the North and South fields denoted 'N' and 'S' respectively; the *XMM-Newton*-2dF survey (Basilakos et al. 2004), filled (brown) rectangles; the *XMM-Newton* COSMOS survey measured by Miyaji et al. (2007), are shown by filled (green) triangles, with the 'SFT' (0.5-2 kev), 'MED' (2-4.5 keV) and 'UHD' (4.5-10 keV) band measurements denoted as S, M and U respectively. Very recent measurements from Gilli et al. (2008, in prep.), also using the *XMM-Newton* COSMOS survey are given by the open (green) triangle. Our measurement of the X-ray bright SDSS quasars using the *Rosat* All Sky Survey (Anderson et al. 2007) is given by the filled (light blue) diamond.

gular autocorrelation function, $w(\theta)$, of hard, (2-8 keV) X-ray selected sources detected in a $\approx 2\text{deg}^2$ field using a shallow, $(f_X(2\text{-}8 \text{ keV}) \approx 10^{-14} \text{ ergs cm}^{-2} \text{ s}^{-1})$ and contiguous *XMM-Newton* survey. The area surveyed consisted of 13 usable pointings, overlapping that of the 2QZ survey and resulted in the detection of 171 sources. Various models are given in Basilakos et al. (2004, see their Table 1) and for our comparison, we take the r_0 values calculated with using $(\Omega_m, \Omega_\Lambda) = (0.3, 0.7)$, and which either assumes "pure luminosity evolution" (PLE, Boyle et al. 1998) or "luminosity-dependent density evolution" (LDDE, Ueda et al. 2003). As such, the PLE and LDDE models give different mean redshifts of $\bar{z} = 0.45$ and $\bar{z} = 0.75$ respectively for the AGN sample and Basilakos et al. (2004) find $r_0 = 9.0 \pm 2.0 \quad h^{-1}$ Mpc for the PLE model and $r_0 = 13.5 \pm 3 \quad h^{-1}$ Mpc for the LDDE model, fixing the

power-law slope at $\gamma = 2.2$. These observations are given by filled (brown) pentagons in Fig. 12.

Gilli et al. (2005) obtain a sample of nearly 260 AGN in the *Chandra* Deep Field North (CDF-N, Alexander et al. 2003; Barger et al. 2003) and South (CDF-S, Rosati et al. 2002) with spectroscopic redshifts. They report that in both fields the AGN have a $\bar{z} \sim 0.9$ and a median 0.5-10 keV luminosity of $\bar{L}_X \sim 10^{43}$ erg s^{-1}, i.e. in the local Seyfert galaxy luminosity regime. Correlation lengths and slopes of $r_0 = 5.5 \pm 0.6$, $\gamma = 1.50 \pm 0.12$ and 10.3 ± 1.7, $\gamma = 5.5 \pm 0.6$ are found for the CDF-N and CDF-S respectively (Gilli et al. 2005, their Table 2), shown as filled (green) stars in Fig. 12.

Miyaji et al. (2007) make the first measurements of the angular autocorrelation function of X-ray point sources detected by *XMM-Newton* in the $\sim 2\text{deg}^2$ COSMOS field Scoville et al. (2007). The measurements for the 0.5-2 (SFT) 2-4.5

(MED) and 4.5-10 (UHD) keV bands are given in Fig. 12 are given by filled (green) triangles. Very recently, Gilli et al. (2008, in prep.) also report on the spatial clustering of AGN in the COSMOS field, using ~ 550 spectroscopically identified AGN at a median redshift of $z \sim 1$. They find a value of $r_0 = 8.3 \pm 0.4$ h^{-1} Mpc and a power-law slope of $\gamma = 1.89 \pm 0.07$. However, this result is affected by a 40 AGN strong redshift strucutre at $z \sim 0.36$. Hence, upon removing this structure, r_0 drops to ~ 6 h^{-1} Mpc, still similar to that of the previous deep X-ray AGN measurements and this is the value we plot in Fig. 12 as an open (green) triangle.

Motivated by these deep X-ray studies, we use the matched *Rosat* All Sky Survey (RASS) and SDSS catalogues from Anderson et al. (2003, 2007) to examine the X-ray properties of our quasars. In particluar we take the over 6 200 objects found in the Anderson et al. (2007) catalogue and match them the to 30 239 quasars in our $0.3 \leq z \leq 2.2$ UNIFORM sample. 2 717 objects are matched and we note that the bolometric luminosities of the X-ray matched quasars is $L_{\mathrm{bol}} = 2.42 \times 10^{46}$ ergs s^{-1} and thus very similiar to that of the overall UNIFORM quasar sample. This sample has a mean redshift of $\bar{z} = 0.72$ and we can see that optically identified SDSS quasars at this redshift have real-space correlation length of $r_0 = 6 - 7$ h^{-1} Mpc. As a very preliminary study, however, using the $w_p(\sigma)$ measurement from our RASS-DR5Q X-ray matched sample, we find an $r_0 = 14 \pm 2$ h^{-1} Mpc, shown as the filled (light blue) diamond in Fig. 12. These objects are generally very X-ray bright and have a calculated mean 0.1-2.4 keV flux of $f_X = 7.9 \times 10^{-13}$ ergs cm^{-2} s^{-1} and a mean X-ray luminosity of $L_X = 9.6 \times 10^{44}$ ergs s^{-1}. Thus, although the luminosites of the our X-ray quasar and the deep AGN objects may vary by ~ 2 orders of magnitude, it appears that the correlation function is measured to be roughly the same over redshifts $z = 0.5 - 1.1$ (cf. RASS-SDSS, XMM-2df LDDE and XMM-COSMOS UHD measurements). This would strongly contradict the findings of Plionis et al. (2008) who claim to find a trend of correlation length with X-ray luminosity such that our SDSS quasars, in the Soft X-ray band, should have correlation lengths $r_0 > 30$ h^{-1} Mpc. However, we caution again that we are comparing measurements across X-ray bands, these are only initial findings for the RASS-SDSS and this study is prime for substantial follow-up investigations.

5.3 Evolution of Bias

One key reason for investigating the correlation function and its form as a function of redshift, $\xi(s,z)$, is to determine the linear bias, b, where

$$b = \sqrt{\frac{\xi_Q(r)}{\xi_\rho(r)}} \qquad (16)$$

is a simple model that we shall assume holds true on the scales and redshift range under investigation here. We are also assuming here the bias is scale-independent[1]. As such, we follow the method in Croom et al. (2005) and da Ângela

---

[1] We do note however, that the precise way in which galaxies/luminous AGN trace the underlying matter distribution is still poorly understood, with e.g. Blanton et al. (2006), Schulz & White (2006), Smith et al. (2007) and Coles & Erdogdu (2007),

et al. (2008) to determine b and use our redshift-space correlation function $\xi(s,z)$ measurements from Section 4.

The volume-averaged correlation function, $\bar{\xi}$ is defined as

$$\bar{\xi} = \frac{\int_0^s 4\pi s'^2 \xi(s')ds}{\int_0^s 4\pi s'^2 ds} \qquad (17)$$

$$= \frac{3}{s_{\max}^3} \int_{s_{\min}}^{s_{\max}} \xi(s')s'^2 ds. \qquad (18)$$

where $s_{\min} = 1.0$ h^{-1} Mpc is set in practice. Unless explicitly stated otherwise, $s_{\max}$ is always chosen to be 20 h^{-1} Mpc, so that non-linear effects in the sample should be insignificant due to the s^2 weighting and for ease of comparison with Croom et al. (2005) and da Ângela et al. (2008). In the linear regime, the z-space and real-space correlation functions can be given by

$$\bar{\xi}_Q(s,z) = \left(1 + \frac{2}{3}\beta + \frac{1}{5}\beta^2\right)\bar{\xi}_Q(r,z). \qquad (19)$$

Thus, combining equations 16 and 19, and taking into account that $\beta = \Omega_m^{0.55}/b$ leaves us with a quadratic equation in b. We note here that we are assuming a flat, cosmological-constant model and hence Ω_m is raised to the 0.55 (Linder 2005; Guzzo et al. 2008), which is a slight departure from the value of 0.6 usually used to relate β to the bias (though we find this makes virtually no difference to our bias measurements). Solving the quadratic in b leads to

$$b(z) = \sqrt{\frac{\bar{\xi}_Q(s,z)}{\bar{\xi}_\rho(r,z)} - \frac{4\Omega_m^{1.1}(z)}{45}} - \frac{\Omega_m^{0.55}(z)}{3}. \qquad (20)$$

Therefore, we can now use our measured $\bar{\xi}_Q(s,z)$ together with a theoretical model estimate of $\bar{\xi}_\rho(r,z)$ to determine the bias, again assuming that were are dealing with a simple scale-independent bias model.

To estimate $\bar{\xi}_\rho(r,z)$, we follow Myers et al. (2007) and da Ângela et al. (2008), and use the non-linear estimate of $P(k)$ given by Smith et al. (2003). The models of Smith et al. (2003) predict the non-linear power spectrum of dark matter for a range of cold dark matter (CDM) cosmologies over a wide range of scale and we thus Fourier transform these $P(k)$ models, and integrate over $s = 1 - 20$ h^{-1} Mpc to compute $\bar{\xi}_\rho(r,z)$. The cosmological parametres used in these models are $\Omega_{\mathrm{m}} = 0.3$, $\Omega_\Lambda = 0.7$, $\Gamma = 0.17$ and $\sigma_8 = 0.84$. We find the simple form,

$$\bar{\xi}_\rho(r,z) = A\exp(Bz) + C \qquad (21)$$

where $A = 0.20413$, $B = -1.0823$, and $C = 0.0178$ models the evolution of $\bar{\xi}_\rho(r,z)$ extremely well, for 1 h^{-1} Mpc $\leq s \leq 20$ h^{-1} Mpc.

Our value for $b_Q(z)$ from the full SDSS DR5Q UNIFORM sample is $b_Q(z = 1.27) = 2.06 \pm 0.03$ and the values for our redshift sub-samples are shown in Fig. 13 by the filled (black) circles. We estimate our errors by using the variations in $\bar{\xi}(s)$ from our 21 jackknife estimates and then scaling using the number of DD pairs in each redshift slice subsample.

Previous measurements from the 2QZ Survey (filled,

---

suggesting that bias is potentially scale dependent and we note that we do not take this into account in the current analysis
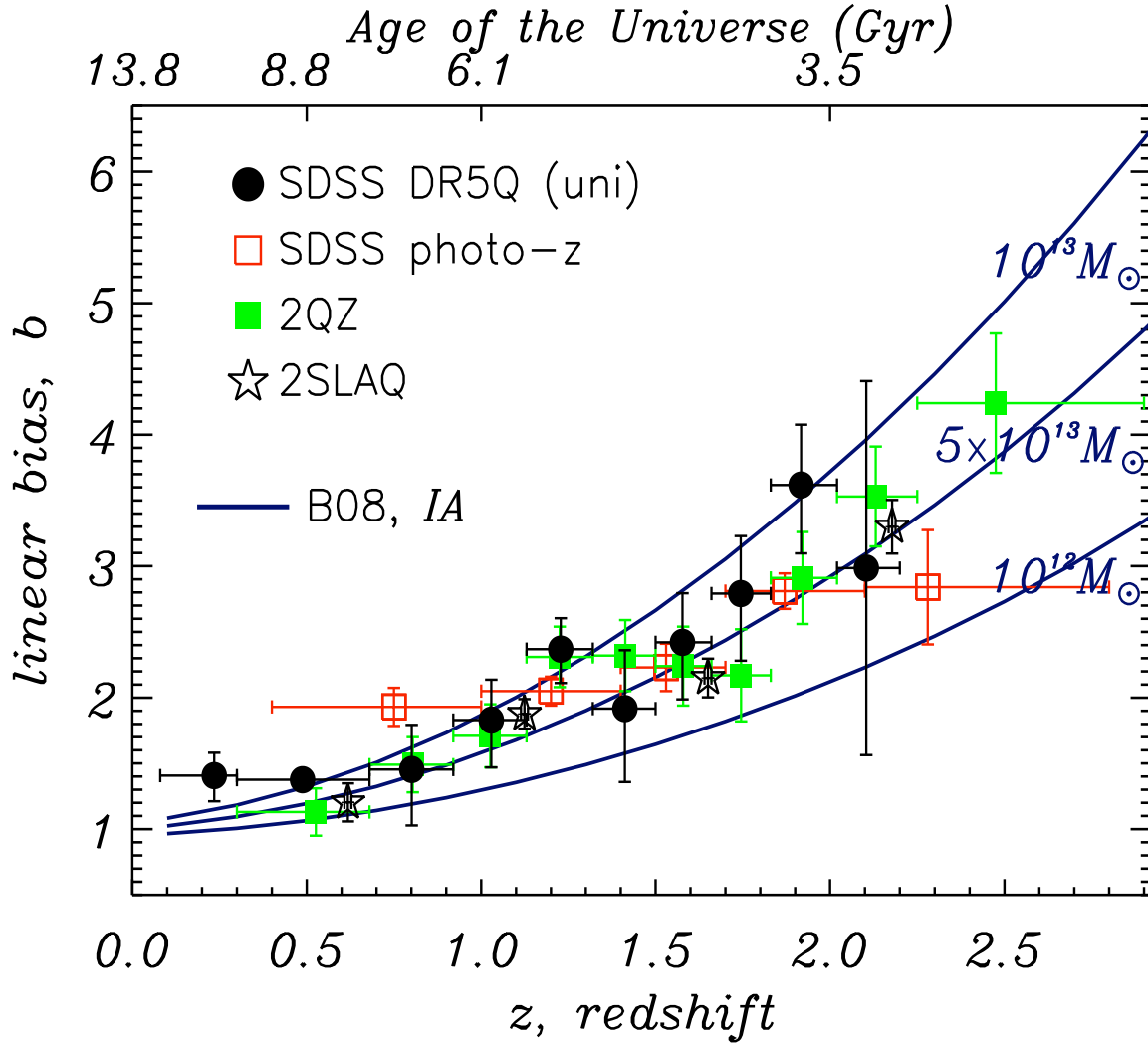
Figure 13. Evolution of the linear bias of quasars, b_Q. with redshift, upto $z = 3$. The filled (black) cirlces, are from the SDSS DR5Q UNIFORM sample (this work); the open (red) squares, from the photometric SDSS quasar measurements (Myers et al. 2006); the filled (green) squares from the 2QZ survey (Croom et al. 2005); the open (black) stars are from the 2SLAQ QSO survey (da Ângela et al. 2008); The lines give dark halo masses from the models of Basilakos et al. (2008).

green circles, Croom et al. 2005), the 2SLAQ QSO Survey (open black stars, da Ângela et al. 2008) and and photometrically selected SDSS quasars (open, red squares, Myers et al. 2007) are again in excellent agreement to our data. Using these bias estimates we can now test against various models.

5.4 Models of bias and dark matter halo mass estimation

We compare our bias measurements with those of two recent models. The first model is that from Basilakos et al. (2008). These authors develope a model based on linear perturbation theory in the matter-dominated epoch. They present a model where the mass-tracer population (i.e. quasars in our cases) evolves according to a $(1 + z)^\nu$ law. There are three general cases: $\nu > 2$ implies merging of dark matter haloes; $\nu < 2$ implies the destruction of dark matter haloes of a particular mass and where $\nu = 2$ is the no-interaction

scenario (where merging and destruction cancel out). These analytical models are then found to compared well against N-body simulations. From these simluations, we are able to evaluate ν, as well as find the dark matter halo mass, at a given z, using linear bias measurements. We plot these models in Fig. 13 for 3 cases of different mass where ν is constant at 2.56, i.e. halo mergers take place,

As can been seen, the mass at which a 'typical SDSS' quasar resides, remains constant (given associated errors) with redshift. Using the models from Basilakos et al. (2008), we obtain that the quasar halo mass remains relatively constant at $M_{DMH} = 5 \times 10^{12} - 1 \times 10^{13} h^{-1} M_\odot$ from redshift $z = 2.2$ to the present day, i.e. over 80% the assumed age of the Universe. Therefore, as dark matter halo masses generally grow in mass with time, the given halo mass for a typical quasar becomes *relatively less massive*, as compared with other haloes at the same epoch, as you approach redshift $z = 0$. This can be thought of as one aspect of cosmic AGN "downsizing". This general term essentially relates a

given objects activity, e.g. star-formation rate, optical or X-ray luminosity, moving to a lower characteristic mass scale as $z \rightarrow 0$ (Pei 1995; Cowie et al. 1996; Ueda et al. 2003; Heckman et al. 2004; Scannapieco et al. 2005; Hasinger et al. 2005; Hasinger 2008).

The second model we compare our data with is that of Hopkins et al. (2007). Full details of the models we use here can be found in that paper, but the limiting factor between model descrimination becomes the dynamic and redshift ranges. As such, we extend our redshift baseline up to $z = 6$ in Figure 14 and now also plot the bias estimates for the high, $z > 2.9$ SDSS quasar clustering measurements of Shen et al. (2007), given by the open (blue) circles. The Hopkins et al. (2007) models are generated and subsequently plotted such that they follow a population of quasars from a survey that has a limiting magnitude of $i = 20.2$, i.e. that of the SDSS high-z selection. Three models are put forward. The first is the default, "Uniform growth" model, which assumes that the SMBH central engine of quasars grow with the quasar Luminsoity Function (QLF) to $z \sim 2$, before "shutting down". In this case, at $z > 2$, the quasar can have multiple epochs of high activity and represents the same systems building hierarchically at these high redshifts. The second model is an "Efficient Feedback" model where the quasar "shuts down" once its quasar phase has ended, even if this is at high, $z > 2$, redshifts. The final model is one of "Maximal Growth", where at $z > 2$, not only the build-up of the QLF contributes to the growth of the SMBH, but also the growth is 'enhanced' by growing proportionally with the host of dark matter halo up until "shut-down" at $z \sim 2$. (Thus all 3 models have the same $z < 2$ behaviour and hence the need for high redshift information).

We see from Fig. 14 that at $i = 20.2$ both the "Uniform Growth" model and the "Efficient Feedback" model reproduce the observed clustering extremely well. Note for both these models at $i = 20.2$, the bias evolution is essentially identical and hence the dotted line is actually under the thin solid line. The "Maximal Growth" model seems to be disfavoured by the quasar data as compared to the other two models, although it cannot be ruled out with current measurements. Caution has to be taken with the $i = 20.2$ models at high redshifts, since due to this magnitude limit, only the very brightest, rarest and potentially most biased objects will be observed.

In an effort to break the "Uniform Growth"-"Efficient Feedback" degeneracy at $i = 20.2$, we plot recent results from studies of high redshift Lyman Break Galaxies (LBGs) from a deep survey by McLure et al. (2008) - given by the solid (grey) triangle in Fig. 14. The "Uniform Growth" and "Effifient Feedback" models are now given as the thick solid line and dotted line respectively and described the bias evolution of an L^* object that could be observed from an essentially infinitely deep survey. We see that the "Uniform Growth" model is now heavily favoured, with this model going straight through the observational point. These result then suggests LBGs could be the progenitors to $z < 2$ quasars, having grown hierarchically, with multiple epochs of quasar activity at high redshifts. However, further investigation into the link between AGN/Quasar activity, the build-up of SBMH mass and the formation and evolution of galaxies using clustering measurements is left to a future investigation (Ross et al., 2008 in prep.).
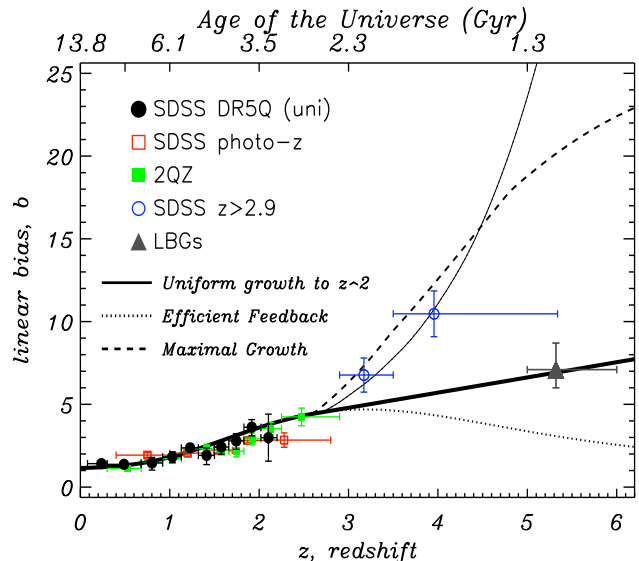

Figure 14. Evolution of the linear bias of quasars, b_Q, with redshift to $z = 6$. Filled (black) cirlces, this work; Filled (green) squares, Croom et al. (2005); Open (red) squares, Myers et al. (2006); Open (blue) circles, Shen et al. (2007); Solid lines show the "Uniform growth" models for a magnitude limited survey of $i = 20.2$ (thin solid line) and an effectively infinitely deep survey (thick solid line). Dashed lines are for the "Efficient feedback" survey (though note at $i = 20.2$ these are identical to the Unifrom growth case. "Maximal growth" at $i = 20.2$ is given by the dashed line. The solid (grey) triangle gives the recent measurements of LBG bias from McLure et al. (2008).

6 CONCLUSIONS

We have used the SDSS Quasar Survey to calculate the 2-point correlation function over $\sim 5000 \deg^2$ of the sky, covering a redshift range of $0 < z \leq 2.9$, thus representing a measurement over the largest volume of the Universe ever sampled (if using our 'PRIMARY' catalogue data). We find that:

• The 2-Point redshift-space correlation function is well described by a single power-law of the form $\xi = (s/s_0)^{-\gamma}$ where $s_0 = 5.95 \pm 0.45 \ h^{-1}$ Mpc and $\gamma = 1.16^{+0.11}_{-0.16}$ over $1 \leq s \leq 25 \ h^{-1}$ Mpc.

• The are relatively strong redshift-space distortions present in the 2-D $\xi(\sigma, \pi)$ measurement. A weak "Fingers of God" measuremment is seen at small-scales, while at large scales, clear distortions are seen, parameterised by a value of $\beta(z = 1.27) = 0.43 \pm 0.1$. This is inline with measurements from previous surveys (e.g. the 2QZ).

• We no evidence for deviation from $\xi(s) = 0$ at scales of $s > 100 \ h^{-1}$ Mpc.

• We do find evidence of weak clustering evolution, with the amplitude of the SDSS quasar correlation fuction increasing wih redshift.

• Using SDSS-RASS matched catalogues and recent results from deep, small area, X-ray surveys, we do not find evidence for a dependence of clustering strength X-ray luminosity, though we caution further investigation is required here.

• Using models to predict dark halo mass, we find that the dark halo mass at which a 'typical SDSS quasar' resides,

remains roughly constant with redshift at $M = 5 \times 10^{12} - 1 \times 10^{13} M_\odot$. Therefore, as dark halo masses grow in mass with time, the typical halo mass for a quasar becomes *relatively less massive*, as compared with other haloes at the same epoch, as you approach redshift $z = 0$. This can be thought of as one aspect of "AGN downsizing".

• We also find from our models that a "Uniform Growth" model, where SMBHs/Quasasr grow hierarchically, with multiple epochs of quasar activity at high redshifts, fits the current observation data well, out to $z = 6$

• Finally, we tentatively suggest that high, $z = 5 - 6$ LBGs are the progenitors of low, $z < 2$ redshift quasars and AGN.

In Shen et al. (2008, in prep.) we shall continue our investigations into the SDSS Quasar population and study the clustering properties of DR5 quasars as a function of luminosity, virial mass, colour and radio-loudness.

Looking further afield, even with the dramatic increase in data that surveys such as the 2QZ and SDSS have provided, the desire to increase dynamic range continues. For instance, due to the steepness of the faint-end of the quasar luminosity-function, low-luminosity quasars should be relatively plentiful, as long as one can identify these objects. This will be a strong challenge for the next-generation of quasar redshift surveys but one that will lead again to another significant increase in our understanding of quasars, supermassive black holes, galaxy formation and evolution and the properties of the Universe.

APPENDIX A: SDSS TECHNICAL DETAILS

A1   The Catalogue Archive Server

The SDSS database can be interrogated through the Catalog Archive Server[2] (CAS) using standard Structured Query Language (SQL) queries. When querying the CAS, you have a choice to query either the `best` database or the `target` database for a given Data Release (in our case, DR5). The difference between the `best` and `target` is that the former database contains information on all the photometric and spectroscopic objects obtained using the latest versions (and i.e. the "best") of the data reduction and analysis pipelines, (Section 3, Abazajian et al. 2004). The `target` database however, contains the information on objects at the time when the targeting algorithm pipelines were run, which, in general, pre-dates the current `best` data by a significant amount. Thus, an objects properties, such as magnitude or colour, can be different between target allocation and the most recent data processing. This of course can lead to objects changing their status to either be included or excluded from a given selection. More details regarding the CAS, `best` and `target` are given in the relevant SDSS Data Release papers (Stoughton et al. 2002; Abazajian et al. 2004; Adelman-McCarthy et al. 2007).

Thus, in order to create a statistical data sample, or indeed to mimic it for a comparative 'random' sample, we need to know the properties of our chosen objects *at the time of targetting*, i.e. which objects were selected as quasar candidates. The DR5Q catalog gives information from both the `best` and `target` databases, however, we only use information from `target` unless explicitly stated otherwise.

A2   SDSS Survey Geometry

For our purposes, we define three functions, which have dependence on angular position in the sky only.

• Coverage Completeness, $f_c(\theta)$. The coverage completeness is simply the ratio of the number of quasar targets that are assigned a fibre to the overall number of quasar candidates in a given area, expressed as a percentage. The natural area for our purposes, shall be a "sector" (as described below).

• Spectroscopic Completeness, $f_s(\theta)$. This is the ratio of the number of high-quality spectra obtained, where there is sufficient confidence that the objects true redshift has been measured.

• Quasar Fraction, $f_q(\theta)$. This is simply the fraction of the number of high-quality spectra that do indeed turn out to be high-redshift quasars (as opposed to e.g. stars in our Galaxy).

An 'overall completeness', f_O, is then easily defined as $f_O = f_q \times f_s \times f_c$. We justify the assumption that these functions depend only on the angular position by referring to the checks made in Vanden Berk et al. (2005), who state that, when dealing with a well-defined statistical sample, the SDSS Quasar Survey is $\sim 95\%$ complete.

---

[2] http://cas.sdss.org

As such, we run various SQL queries on the SDSS CAS. The first query (Appendix A3) simply asks the CAS to return all the objects in the Photometric database that were targetted as being "primary" candidate quasars. When run on DR5, this returns 203 185 unique objects, from the PhotoObjAll table.

We next calculate which 'Primary PhotoObjAll' objects (POAs) fall within the spectroscopic survey plate boundaries. We use the parameter file, `maindr5spectro.par` found on the SDSS website[3], which contains the plate number, Modified Julian Date (MJD), and plate centre (in J2000 Right Ascension and Declination). 1 278 plate details consisting of the SDSS DR5 are given in this file. Note, we do not use any of the "Extra", "Special", or "ExtraSpecial" plates for our analysis and warn that the PlateX table found in the CAS does not explicitly make these plate distinctions. We find there are 145,524 POA objects that fall within 1.49 degrees of a given DR5 plate centre, noting that since plates overlap due to the tiling scheme, an object can be in more than one plate.

Of these 145,524 objects (which recall were all photometrically labelled as 'primary quasars'), we would next like to know, how many were *(a)* designated as spectroscopic ("tilable") targets by the process of 'Tiling' and *(b)* how many of these Targets were allocated fibres. Note here that the difference in the SDSS between "tiles" and plates is that a tile is a 1.49 degree radius circle on the sky determined by tiling, and which contains the locations of up to 592 tilable targets and other science targets (the other 48 fibres are assigned to calibration targets). For each tile, one, or more, physical aluminum plates will be created. The plates will have holes drilled in them for fibres to be plugged, in order to observe the tiled targets. Thus, one tile can have several Plates, with the plates having common centres.

The design of the SDSS survey with regards to the tiling procedure is described in detail by Blanton et al. (2003)[4] and its goal is to maximise the probability of a target being fibred. Furthermore, because of the large-scale structure in the quasar/galaxy distribution that is known to exist, an optimal Tiling procedure will cause individual Tiles to overlap with each other. As described in Blanton et al. (2003); Tegmark et al. (2004); Blanton et al. (2005); Percival et al. (2007), a "sector" is defined as a set of spherical polygons (i.e. tile overlap regions) that could have only been observed by a unique combination of tiles and survey "chunks". A 'chunk' is a unit of SDSS imaging data and is a part of an SDSS 'stripe', which is a 2.5 degree wide cylindrical segment aligned at a great circle between the survey poles. Thus a slight complication arises in that plates, sectors and plate centres deal with α and δ coordinates, whereas chunks are defined by the survey coordinates η and λ (with the coordinate transformations given in Section 3.2.2 of Stoughton et al. 2002). Again, the SDSS website, `www.sdss.org` and the relevant data release papers have complete details. These sectors are thus the appropriate regions on which to define the completeness of our sample and survey.

Using the RegionID field in the TARGET table (which gives the sector identification number if set, zero otherwise)
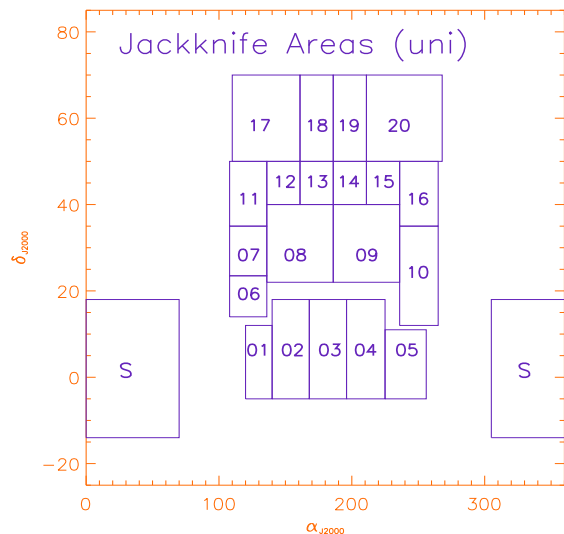
Figure B1. Geometry of the SDSS DR5Q Jackknife areas. Note the areas were chose such that they folled the overall geometry of the SDSS Quasar survey and that the number of quasars removed in each field was approximately equal.

we match the positions (R.A.'s and Decs) of objects in TARGET to those that are in PhotoObjAll and the DR5Q.

From here we figure out sector completenesses and the angular mask of the SDSS DR5 Survey. We also note that the imaging 'chunks' also play a role in defining the geometry of the SDSS survey since a chunk is $2.5°$ wide, whereas a tile is $3.0°$ wide and thus there will be regions that have been tiled but which have no imaging data and thus no spectroscopic targets to contribute to our sample. Note, we do not include the effect of that targets less than 100 arcsec from the tile center are excluded.

APPENDIX B: JACKKNIFE ERRORS

Here we follow Scranton et al. (2002, §§3.4.5, 11.3 and their Eq. 10), Zehavi et al. (2002, §3.4 and equation 7) and Myers et al. (2007, Appendix A) in order to calculate the jackknife error estimates on our quasar clustering data. We also note the recent work of Loh (2008) to this specific issue.

Myers et al. (2007) estimate errors using an "inverse variance" weighted jackknife technique. This method divides the data into N sub-samples and then recalculates the given statistic (e.g. $\xi(s)$) using the Landy-Szalay esimator 5, *leaving out* one sub-sample area at one time. Therefore, following the convention of Myers et al. (2007), if we denote subsamples by the subscript L and recalculate $\xi(s)_L$ in each jackknife realization via equation 5 then the inverse-variance-weighted covariance matrix , C_{ij} can be generated as

$$C_{ij} = C(s_i, s_j) = \sum_{L=1}^{N} \sqrt{\frac{RR_L(s_i)}{RR(s_i)}} \left[\xi_L(s_i) - \xi(s_i) \right] \sqrt{\frac{RR_L(s_j)}{RR(s_j)}} \left[\xi_L(s_j) - \xi(s_j) \right] \quad \text{(B1)}$$

where, ξ denotes the correlation function for all data and ξ_L denotes the correlation function for subsample L. Jackknife errors σ_i are obtained from the diagonal elements ($\sigma_i^2 =$
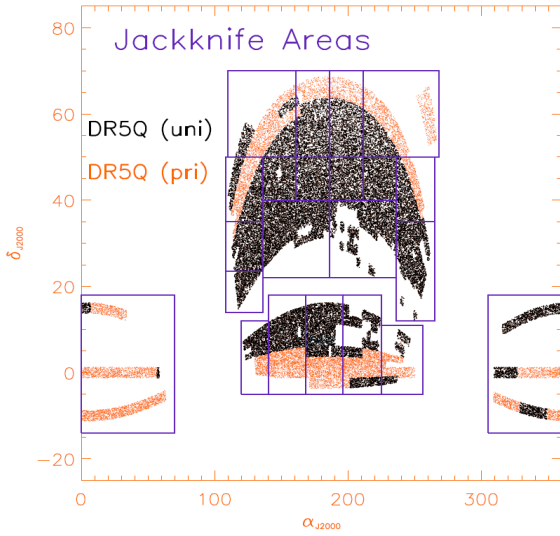
Figure B2. Geometry of the SDSS DR5Q Jackknife areas, now showing the location of the DR5Q PRIMARY, orange/grey dots and the UNIFORM, black dots, samples. Note the sparse coverage of the UNIFORM sample in the Southern Stripes.
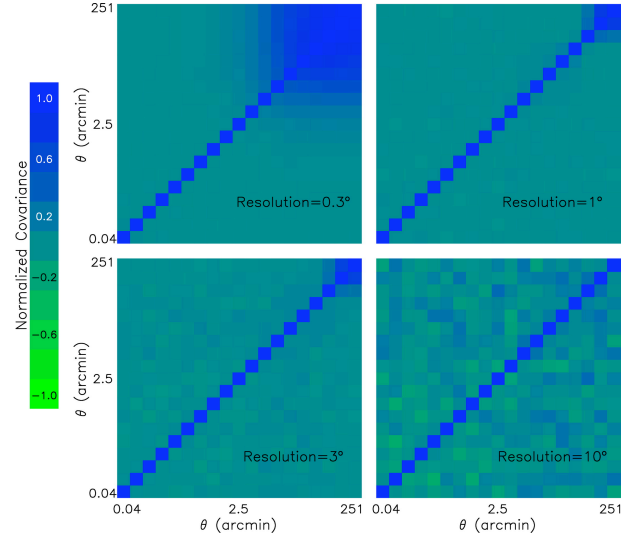

Figure B3. The normalised Covariance Matrix, (a.k.a. the Regression Matrix) for $\xi(s)$ from jackknife error anaylsis on 20 sub-samples of the UNIFORM DR5Q. [**PLACE HOLDER FROM MYERS et al. (2007, ApJ, 658, 85)**]

| Region	RA min	RA max	Dec min	Dec max	No. of Quasars	No. of Randoms
N01	120.	140.	-5.	12.	29 445	870 558
N02	140.	168.	-5.	15.	28 445	841 193
N03	168.	196.	-5.	18.	27 904	825 442
N04	196.	225.	-5.	18.	28 717	846 926
N05	225.	256.	-5.	11.	29 891	879 837
N06	108.	136.	14.	23.5	29 614	873 778
N07	108.	136.	23.5	35.	28 646	845 871
N08	136.	186.	22.	40.	26 942	798 307
N09	186.	236.	22.	40.	27 957	820 491
N10	236.	265.	12.	35.	28 253	831 920
N11	108.	136.	35.	50.	29 003	856 576
N12	136.	161.	40.	50.	28 875	855 021
N13	161.	186.	40.	50.	28 857	853 908
N14	186.	211.	40.	50.	28 917	854 055
N15	211.	236.	40.	50.	28 924	854 070
N16	236.	265.	35.	50.	29 246	863 221
N17	110.	161.	50.	70.	29 253	863 420
N18	161.	186.	50.	70.	28 899	853 792
N19	186.	211.	50.	70.	28 911	853 175
N20	211.	268.	50.	70.	29 404	868 561
S	0∨305	70∨360	-14	18	28 675	842 497
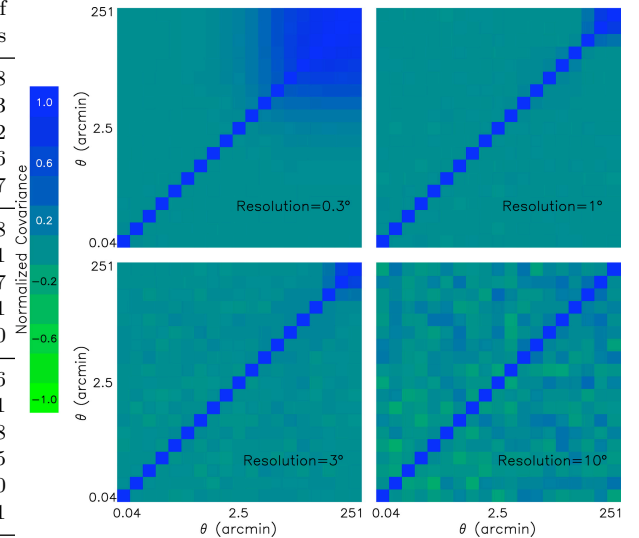
Figure B4. The normalised Covariance Matrix, (a.k.a. the Regression Matrix) for $\xi(s)$ from jackknife error anaylsis on 20 sub-samples of the UNIFORM DR5Q. [**PLACE HOLDER FROM MYERS et al. (2007, ApJ, 658, 85)**]

C_{ii}), and the normalized covariance matrix, also known as the regression matrix, is

$$|C| = \frac{C_{ij}}{\sigma_i \sigma_j} \qquad (B2)$$

We divide the sample into 20 sub-samples, with, the number of subdivisions is chosen such that each represents a cosmologically significant volume, while retaining sufficient numbers of objects that shot noise will not dominate any subsequent analysis. The detailed boundaries of the sub-samples are given in Table B and Figures B1 and B2.

We find, as in previous quasar clustering work Shanks & Boyle (e.g. 1994); Croom & Shanks (e.g. 1996), that Poisson errors are a good descritpion on scales where $N_q \lesssim DD_q$, where N_q is the number of quasars in a given sample and DD_q is the number of quasar pairs. While at scales where $N_q > DD$, the Poisson error tends to underestimate the Jackknife error, see B5. We note that the scale where $N_q \approx DD_q$ is $\sim 70 \ h^{-1}$ Mpc for the SDSS, UNIFORM Quasar sample and that above this scale, the Poisson error estimate is approximately double that of the Jackknifer error estimate.
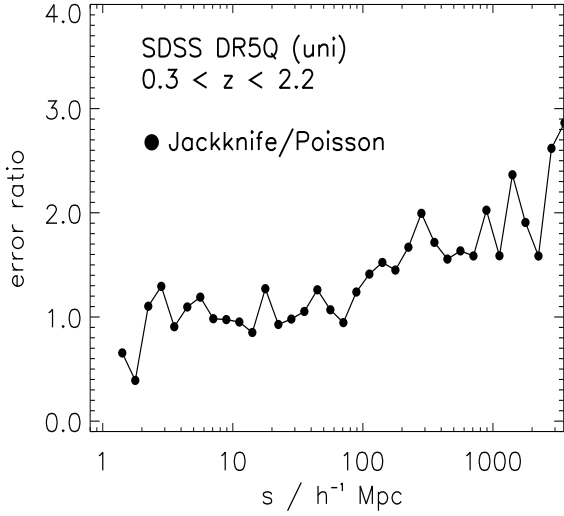
Figure B5. Comparison of Poisson and Jackknife errors for the UNIFORM DR5 Quasar sample. Note the ratio between the Poisson and Jackknife errors is very close to one at $s \lesssim 70$ h^{-1} Mpc scales, while at $s \gtrsim 70$ h^{-1} Mpc, the Poisson errors is $\sim$ double that of the Jackknifes.
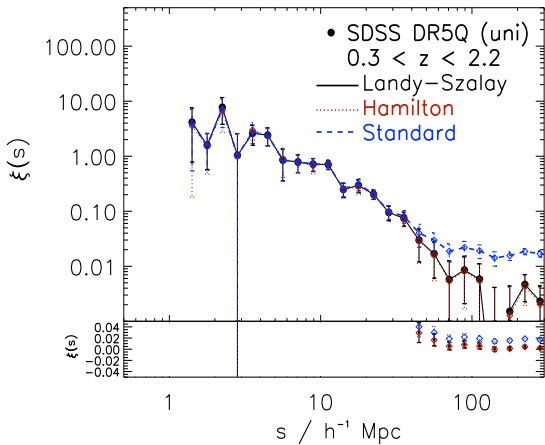

Figure C1. The SDSS DR5 Quasar $\xi(s)$ for the UNIFORM sample using the 'Standard', Hamilton and Landy-Szalay estimators.

APPENDIX C: SYSTEMATICS IN THE SDSS QUASAR 2PCF.

Here we produce evidence showing how various changes to our data and random methodology described in Sections 2 and 3 affect our main results. We generally report on $\xi(s)$ as this is the most robust of our 2PCF measurements.

C1   Different Estimators for UNIFORM $\xi(s)$

Figures C1, C2 and C3 show the redshift-space 2PCF, $\xi(s)$ for the UNIFORM sample, using the different estimators of Davis & Peebles (1983), Hamilton (1992) and Landy & Szalay (1993). While the trend for the two estimators that use random-random (RR) pair counts are in extremely good agreement, the 'Standard' estimator, seems to have too much power on large, $s \geq 40$ h^{-1} Mpc scales. The Davis-
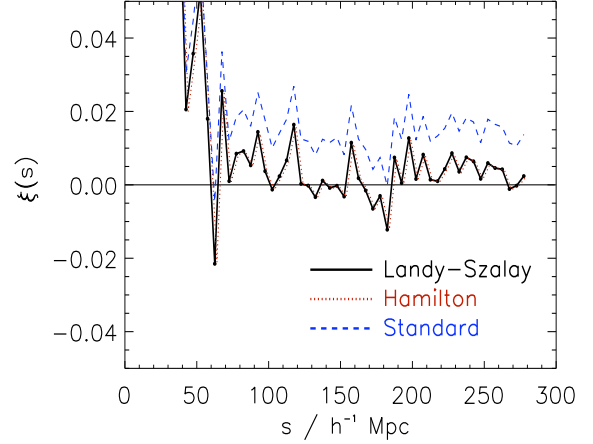

Figure C2. The SDSS DR5 Quasar $\xi(s)$ for the UNIFORM sample using the 'Standard', Hamilton and Landy-Szalay estimators.
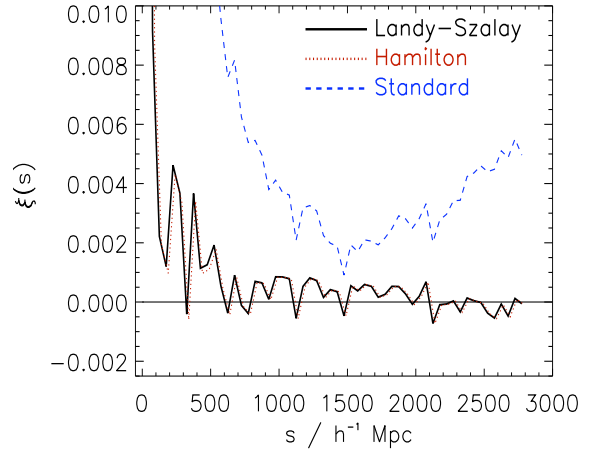

Figure C3. The SDSS DR5 Quasar $\xi(s)$ for the UNIFORM sample using the 'Standard', Hamilton and Landy-Szalay estimators.

Peebles is less robust to errors in the estimation of mean density, which would explain this discrepency.

C2   PRIMARY vs. UNIFORM $\xi(s)$

Figure C4 shows the difference in the redshift-space correlation function, $\xi(s)$, for the PRIMARY sample, versus that of the UNIFORM sample. Again we see excellent agreement of the two samples at small $s \leq 20$ h^{-1} Mpc scales, but the PRIMARY sample exhibits a higher clustering strength at large-scales, $s \geq 40$ h^{-1} Mpc. Althought this trend was seen in an unpublished calculation on the SDSS DR3 Quasar sample, we currently do not believe it to be a real affect but it remains unexplained at this point.

C3   UNIFORM $z < 2.2$ vs. $z < 2.9$ $\xi(s)$

Figure C5 shows the redshift-space 2-point correlation function $\xi(s)$ for the UNIFORM sample with the high-redshift cut-off being changed from $z \leq 2.2$ to $z \leq 2.9$.
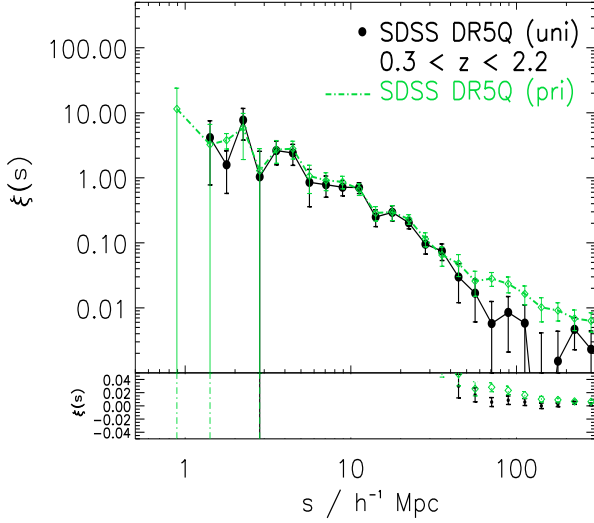
Figure C4. The SDSS DR5 Quasar $\xi(s)$ the PRIMARY and UNIFORM samples. The lower panel shows the behaviour of the Uniform $\xi(s)$ near zero on a linear scale
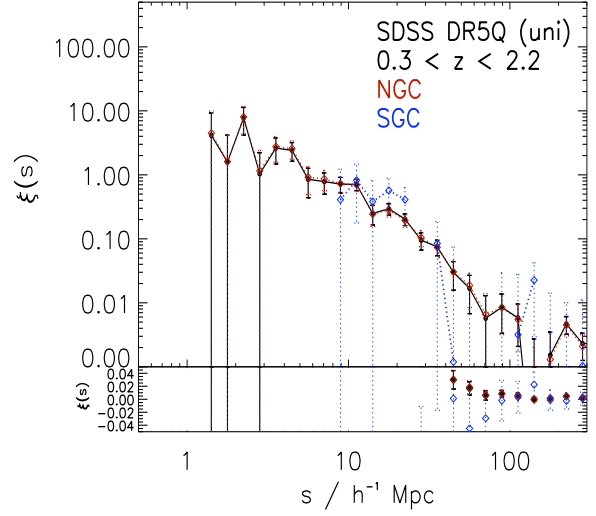

Figure C6. The SDSS DR5 Quasar $\xi(s)$ the UNIFORM sample with the sample split into the NCG and SCG.
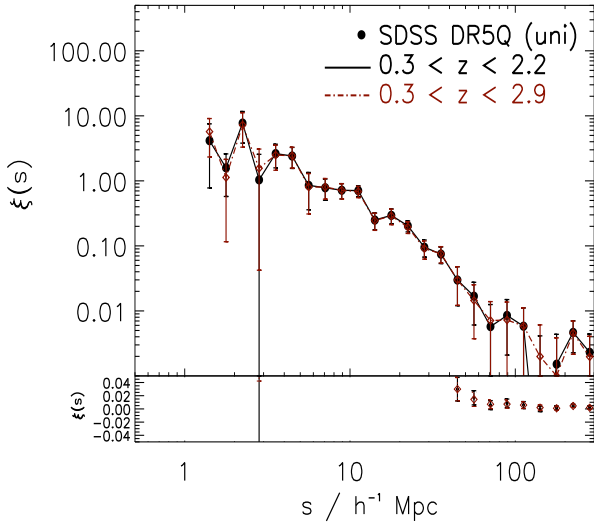

Figure C5. The SDSS DR5 Quasar $\xi(s)$ the PRIMARY and UNIFORM samples. The lower panel shows the behaviour of the Uniform $0.3 < z < \xi(s)$ near zero on a linear scale

Figure C7. The SDSS DR5 Quasar $\xi(s)$ the UNIFORM and PRIMARY sample both including solid (green) line and excluding, dashed (red) line bad imaging fields

C4   UNIFORM NGC vs. SGC $\xi(s)$

Figure C6 shows the redshift-space 2-point correlation function $\xi(s)$ for the UNIFORM sample, split into quasars from the North Galactic Cap (NGC) and the South Galactic Cap (SGC). Note the data is heavily dominated by the NGC in the UNIFORM sample.

C5   PRIMARY and "Bad Fields" $\xi(s)$

Figure C7 shows the redshift-space 2-point correlation function $\xi(s)$ for the PRIMARY sample, including solid (green) and excluding dashed (red) lines, the "Bad Fields" as defined by Shen et al. (2007).
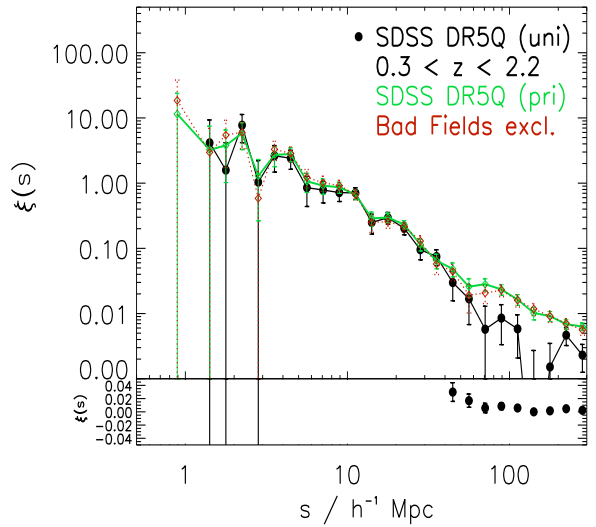
C6   PRIMARY from Single and Multiple Plates $\xi(s)$

Figure C8 shows the redshift-space 2-point correlation function $\xi(s)$ for the PRIMARY sample with data coming from Single (red) or Multiple (blue) plates.

C7   PRIMARY and "Empty" Sectors

Figure C9 shows the redshift-space 2-point correlation function $\xi(s)$ for the PRIMARY sample with "Empty Sectors" (those with no primary quasar targets at all), having 1, 0.5 or 0 completeness. There are 1983 "Empty" sectors contributing 93 deg^2 to the DR5Q.
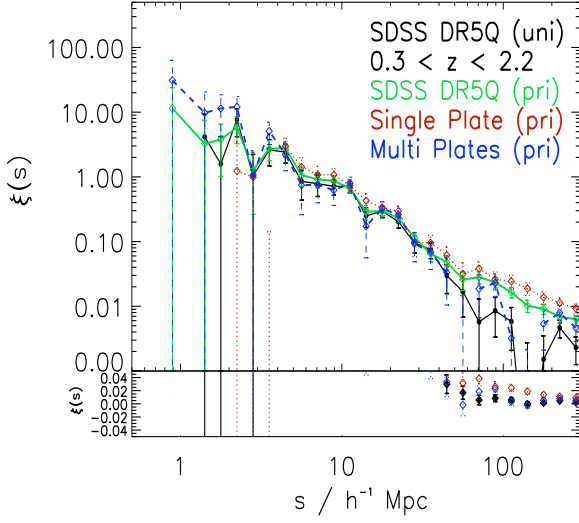
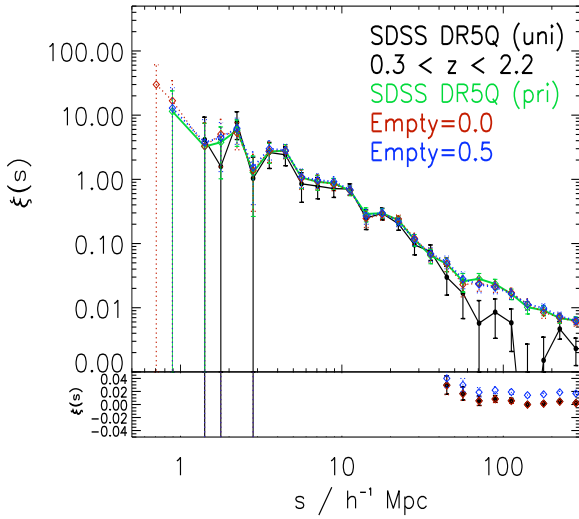**Figure C8.** The PRIMARY sample $\xi(s)$ with data coming from Single (red) or Multiple (blue) plates.

Figure C10.

Figure C9. The SDSS DR5 Quasar $\xi(s)$ the UNIFORM sample with the sample split into the NCG and SCG.

C8 $w_p(\sigma)$, varying $\pi_{\max}$ limits

Figure C10 shows the projected correlation function $\xi(s)$ for the SDSS DR5Q Uniform samples, $0.30 < z < 2.2$, varying $\pi_{\max}$ from equation.

REFERENCES

Abazajian K., et al., 2003, AJ, 126, 2081
Abazajian K., et al., 2004, AJ, 128, 502
Adelman-McCarthy J. K., et al., 2007, ApJS, 172, 634
Alexander D. M., et al., 2003, AJ, 126, 539
Anderson S. F., et al., 2003, AJ, 126, 2209
Anderson S. F., et al., 2007, AJ, 133, 313
Arp H., 1970, AJ, 75, 1
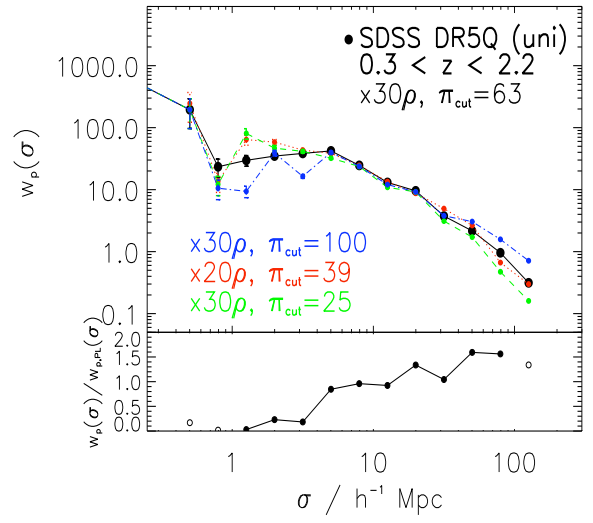Baes M., Buyle P., Hau G. K. T., Dejonghe H., 2003, MN-RAS, 341, L44

Barger A. J., et al., 2003, AJ, 126, 632
Basilakos S., Georgakakis A., Plionis M., Georgantopoulos I., 2004, ApJ Lett., 607, L79
Basilakos S., Plionis M., Ragone-Figueroa C., 2008, ApJ, 678, 627
Becker R. H., White R. L., Helfand D. J., 1995, ApJ, 450, 559
Blanton M. R., Eisenstein D., Hogg D. W., Zehavi I., 2006, ApJ, 645, 977
Blanton M. R., et al., 2005, AJ, 129, 2562
Blanton M. R., Lin H., Lupton R. H., Maley F. M., Young N., Zehavi I., Loveday J., 2003, AJ, 125, 2276
Boyle B. J., Georgantopoulos I., Blair A. J., Stewart G. C., Griffiths R. E., Shanks T., Gunn K. F., Almaini O., 1998, MNRAS, 296, 1
Boyle B. J., Shanks T., Croom S. M., Smith R. J., Miller L., Loaring N., Heymans C., 2000, MNRAS, 317, 1014
Brandt W. N., Hasinger G., 2005, ARA&A, 43, 827
Coil A. L., Hennawi J. F., Newman J. A., Cooper M. C., Davis M., 2007, ApJ, 654, 115
Coles P., Erdogdu P., 2007, Journal of Cosmology and Astro-Particle Physics, 10, 7
Coles P., Lucchin F., 2002, Cosmology: The Origin and Evolution of Cosmic Structure, Second Edition. Cosmology: The Origin and Evolution of Cosmic Structure, Second Edition, by Peter Coles, Francesco Lucchin, pp. 512. ISBN 0-471-48909-3. Wiley-VCH , July 2002.
Cowie L. L., Songaila A., Hu E. M., Cohen J. G., 1996, AJ, 112, 839
Croom S. M., et al., 2005, MNRAS, 356, 415
Croom S. M., et al., 2008, MNRAS, in prep., 415
Croom S. M., Shanks T., 1996, MNRAS, 281, 893
Croom S. M., Shanks T., Boyle B. J., Smith R. J., Miller L., Loaring N. S., Hoyle F., 2001, MNRAS, 325, 483
Croom S. M., Smith R. J., Boyle B. J., Shanks T., Miller L., Outram P. J., Loaring N. S., 2004, MNRAS, 349, 1397
da Ângela J., et al., 2008, MNRAS, 383, 565
da Ângela J., Outram P. J., Shanks T., Boyle B. J., Croom S. M., Loaring N. S., Miller L., Smith R. J., 2005, MN-RAS, 360, 1040

Davis M., et al., 2003, in Guhathakurta P., ed., Discoveries and Research Prospects from 6- to 10-Meter-Class Telescopes II. Vol. 4834 of Proceedings of the SPIE,, Science Objectives and Early Results of the DEEP2 Redshift Survey. pp 161–172

Davis M., Newman J. A., Faber S. M., Phillips A. C., 2001, in Cristiani S., Renzini A., Williams R. E., eds, Deep Fields: The DEEP2 Redshift Survey. p. 241

Davis M., Peebles P. J. E., 1983, ApJ, 267, 465

Eisenstein D. J., et al., 2001, AJ, 122, 2267

Fukugita M., Ichikawa T., Gunn J. E., Doi M., Shimasaku K., Schneider D. P., 1996, AJ, 111, 1748

Gilli R., et al., 2005, Astron. & Astrophys., 430, 811

Gunn J. E., et al., 1998, AJ, 116, 3040

Gunn J. E., et al., 2006, AJ, 131, 2332

Guzzo L., et al., 2008, Nature, 451, 541

Haiman Z., Hui L., 2001, ApJ, 547, 27

Hamilton A. J. S., 1992, ApJ Lett., 385, L5

Hasinger G., 2008, ArXiv e-prints, 808

Hasinger G., Miyaji T., Schmidt M., 2005, Astron. & Astrophys., 441, 417

Hawkins E., et al., 2003, MNRAS, 346, 78

Hawkins M. R. S., Reddish V. C., 1975, Nature, 257, 772

Heckman T. M., Kauffmann G., Brinchmann J., Charlot S., Tremonti C., White S. D. M., 2004, ApJ, 613, 109

Hennawi J. F., et al., 2006, AJ, 131, 1

Hogg D. W., Finkbeiner D. P., Schlegel D. J., Gunn J. E., 2001, AJ, 122, 2129

Hopkins P. F., Hernquist L., Cox T. J., Kereš D., 2008, ApJS, 175, 356

Hopkins P. F., Lidz A., Hernquist L., Coil A. L., Myers A. D., Cox T. J., Spergel D. N., 2007, ApJ, 662, 110

Hoyle F., Outram P. J., Shanks T., Boyle B. J., Croom S. M., Smith R. J., 2002, MNRAS, 332, 311

Iovino A., Shaver P. A., 1988, ApJ Lett., 330, L13

Ivezić Ž., et al., 2004, Astronomische Nachrichten, 325, 583

Kaiser N., 1987, MNRAS, 227, 1

Kerscher M., Szapudi I., Szalay A. S., 2000, ApJ Lett., 535, L13

Kundic T., 1997, ApJ, 482, 631

La Franca F., Andreani P., Cristiani S., 1998, ApJ, 497, 529

Landy S. D., Szalay A. S., 1993, ApJ, 412, 64

Lidz A., Hopkins P. F., Cox T. J., Hernquist L., Robertson B., 2006, ApJ, 641, 41

Linder E. V., 2005, Phys. Rev. D, 72, 043529

Loh J. M., 2008, ApJ, 681, 726

Lupton R., Gunn J. E., Ivezić Z., Knapp G. R., Kent S., 2001, in Harnden Jr. F. R., Primini F. A., Payne H. E., eds, Astronomical Data Analysis Software and Systems X Vol. 238 of Astronomical Society of the Pacific Conference Series, The SDSS Imaging Pipelines. p. 269

Lynden-Bell D., 1969, Nature, 223, 690

Martínez V. J., Saar E., 2002, Statistics of the Galaxy Distribution. Chapman & Hall/CRC

Martini P., Weinberg D. H., 2001, ApJ, 547, 12

McLure R. J., Cirasuolo M., Dunlop J. S., Foucaud S., Almaini O., 2008, ArXiv e-prints, 805

Miyaji T., et al., 2007, ApJS, 172, 396

Mountrichas G., Shanks T., 2007, MNRAS, 380, 113

Myers A. D., Brunner R. J., Nichol R. C., Richards G. T., Schneider D. P., Bahcall N. A., 2007, ApJ, 658, 85

Myers A. D., Brunner R. J., Richards G. T., Nichol R. C., Schneider D. P., Bahcall N. A., 2007, ApJ, 658, 99

Myers A. D., et al., 2006, ApJ, 638, 622

Myers A. D., Outram P. J., Shanks T., Boyle B. J., Croom S. M., Loaring N. S., Miller L., Smith R. J., 2005, MNRAS, 359, 741

Myers A. D., Richards G. T., Brunner R. J., Schneider D. P., Strand N. E., Hall P. B., Blomquist J. A., York D. G., 2008, ApJ, 678, 635

Oke J. B., Gunn J. E., 1983, ApJ, 266, 713

Osmer P. S., 1981, ApJ, 247, 762

Outram P. J., Hoyle F., Shanks T., Boyle B. J., Croom S. M., Loaring N. S., Miller L., Smith R. J., 2001, MNRAS, 328, 174

Padmanabhan N., White M., Norberg P., Porciani C., 2008, ArXiv:0802.2105

Peacock J. A., 1999, Cosmological Physics. Cosmological Physics, by John A. Peacock, pp. 704. ISBN 052141072X. Cambridge, UK: Cambridge University Press, January 1999.

Peacock J. A., et al., 2001, Nature, 410, 169

Peebles P. J. E., 1973, ApJ, 185, 413

Peebles P. J. E., 1980, The Large-Scale Structure of the Universe. Princeton University Press.

Peebles P. J. E., 1993, Principles of physical cosmology. Princeton Series in Physics, Princeton, NJ: Princeton University Press, —c1993

Pei Y. C., 1995, ApJ, 438, 623

Percival W. J., et al., 2007, ApJ, 657, 645

Pier J. R., Munn J. A., Hindsley R. B., Hennessy G. S., Kent S. M., Lupton R. H., Ivezić Ž., 2003, AJ, 125, 1559

Plionis M., Rovilos M., Basilakos S., Georgantopoulos I., Bauer F., 2008, ApJ Lett., 674, L5

Porciani C., Magliocchetti M., Norberg P., 2004, MNRAS, 355, 1010

Porciani C., Norberg P., 2006, MNRAS, 371, 1824

Rees M. J., 1984, ARA&A, 22, 471

Richards G. T., et al., 2001, AJ, 122, 1151

Richards G. T., et al., 2002, AJ, 123, 2945

Richards G. T., et al., 2004, ApJS, 155, 257

Richards G. T., et al., 2006, AJ, 131, 2766

Rosati P., Tozzi P., Giacconi R., Gilli R., Hasinger G., Kewley L., Mainieri V., Nonino M., Norman C., Szokoly G., Wang J. X., Zirm A., Bergeron J., Borgani S., Gilmozzi R., Grogin N., Koekemoer A., Schreier E., Zheng W., 2002, ApJ, 566, 667

Ross N. P., et al., 2007, MNRAS, 381, 573

Salpeter E. E., 1964, ApJ, 140, 796

Sánchez A. G., Baugh C. M., Percival W. J., Peacock J. A., Padilla N. D., Cole S., Frenk C. S., Norberg P., 2006, MNRAS, 366, 189

Scannapieco E., Silk J., Bouwens R., 2005, ApJ Lett., 635, L13

Scherrer R. J., Weinberg D. H., 1998, ApJ, 504, 607

Schlegel D. J., Finkbeiner D. P., Davis M., 1998, ApJ, 500, 525

Schneider D. P., et al., 2007, AJ, 134, 102

Schulz A. E., White M., 2006, Astroparticle Physics, 25, 172

Scoville N., et al., 2007, ApJS, 172, 1

Scranton R., et al., 2002, ApJ, 579, 48

Scranton R., et al., 2005, ApJ, 633, 589

Serber W., Bahcall N., Ménard B., Richards G., 2006, ApJ, 643, 68

Shanks T., Boyle B. J., 1994, MNRAS, 271, 753

Shanks T., Fong R., Boyle B. J., Peterson B. A., 1987, MNRAS, 227, 739

Shanks T., Fong R., Green M. R., Clowes R. G., Savage A., 1983, MNRAS, 203, 181

Shen Y., et al., 2007, AJ, 133, 2222

Smith J. A., et al., 2002, AJ, 123, 2121

Smith R. E., et al., 2003, MNRAS, 341, 1311

Smith R. E., Scoccimarro R., Sheth R. K., 2007, Phys. Rev. D, 75, 063512

Spergel D. N., et al., 2007, ApJS, 170, 377

Steffen A. T., Barger A. J., Cowie L. L., Mushotzky R. F., Yang Y., 2003, ApJ Lett., 596, L23

Stoughton C., et al., 2002, AJ, 123, 485

Strauss M. A., et al., 2002, AJ, 124, 1810

Tegmark M., et al., 2004, ApJ, 606, 702

Tucker D. L., et al., 2006, Astronomische Nachrichten, 327, 821

Ueda Y., Akiyama M., Ohta K., Miyaji T., 2003, ApJ, 598, 886

Vanden Berk D. E., et al., 2005, AJ, 129, 2047

Wake D. A., et al., 2004, ApJ Lett., 610, L85

Wright E. L., 2006, PASP, 118, 1711

Wyithe J. S. B., Loeb A., 2005, ApJ, 621, 95

Wyithe J. S. B., Padmanabhan T., 2006, MNRAS, 366, 1029

York D. G., et al., 2000, AJ, 120, 1579

Zehavi I., Blanton M. R., Frieman J. A., Weinberg D. H., Waddell P., Yanny B., York D. G., 2002, ApJ, 571, 172